



# CHORUS

This is the accepted manuscript made available via CHORUS. The article has been published as:

## Enhanced sideband responses in a PT-symmetric-like cavity magnomechanical system

Sai-Nan Huai, Yu-Long Liu, Jing Zhang, Lan Yang, and Yu-xi Liu

Phys. Rev. A **99**, 043803 — Published 4 April 2019

DOI: [10.1103/PhysRevA.99.043803](https://doi.org/10.1103/PhysRevA.99.043803)

# Enhanced sidebands responses in $\mathcal{PT}$ -symmetric-like cavity magnomechanical system

Sai-Nan Huai,<sup>1</sup> Yu-Long Liu,<sup>1,\*</sup> Jing Zhang,<sup>2,3</sup> Lan Yang,<sup>4</sup> and Yu-xi Liu<sup>1,3,†</sup>

<sup>1</sup>*Institute of Microelectronics, Tsinghua University, Beijing 100084, China*

<sup>2</sup>*Department of Automation, Tsinghua University, Beijing 100084, China*

<sup>3</sup>*Beijing National Research Center for Information Science and Technology (BNRist), Beijing 100084, China*

<sup>4</sup>*Department of Electrical and Systems Engineering,  
Washington University, St. Louis, Missouri 63130, USA*

(Dated: March 18, 2019)

Based on the cavity magnomechanical system, which consists of a microwave cavity and a small ferromagnetic sphere, we propose a scheme to construct a parity-time ( $\mathcal{PT}$ ) symmetric-like system formed by the active magnon mode and passive cavity mode. The effective gain of the magnon mode is achieved by resonantly driving the yttrium iron garnet (YIG) sphere and can be modulated by the power of the driving field. We show the  $\mathcal{PT}$ -symmetric phase transition following the variation of magnon-photon coupling strength in microwave regime. We find that the transmission amplitudes and time delays on the first- and second-order sidebands in the  $\mathcal{PT}$ -symmetric-like system can be enhanced for three to four orders, compared to the magnomechanical system, once the magnon-photon coupling strength is tuned to the critical point in the broken- $\mathcal{PT}$  symmetry regime. Particularly, we also show the switching between different transmission spectra (amplification or magnomechanically induced absorption) and time delay (positive or negative) on the first-order Stokes sideband, can be achieved by modulating the power of the control field, cavity-waveguide coupling parameter and magnon-photon coupling strength. Our study shows that the cavity magnomechanical system is a promising platform for exploring  $\mathcal{PT}$ -symmetric-like paradigms in microwave field, and a good candidate for the microwave control on both the first- and high-order sidebands simultaneously. Our study may inspire further applications in frequency combs and low-power magnomechanical amplifier.

## I. INTRODUCTION

The non-Hermitian Hamiltonian, which is related to parity-time ( $\mathcal{PT}$ ) symmetry and exhibits real spectra, has recently attracted extensive attentions [1–3].  $\mathcal{PT}$  symmetry in non-Hermitian Hamiltonian has been manifested in various physical systems, ranging from photonics [4–17], electronics [20–23], to acoustics [24–28] and phononics [29–31]. Extensive researches show that optical systems provide the most fertile ground, where  $\mathcal{PT}$ -related phenomena can be theoretically studied and experimentally realized.  $\mathcal{PT}$  symmetry has been widely applied to optical communication, signal processing and propagation, including the enhancement of optomechanically-induced transparency [32, 33], absorption [34] and amplification [35], nonreciprocal light propagation [36], unidirectional invisibility [37–39]. Besides, it is also useful for enhancing nonlinearity [40, 41] to realize, e.g., optomechanical chaos [42], laser absorber [43], coherent perfect absorber [44], sensors [45–47], and other nonlinear effects [48–50].

Based on the similarity between the optical and microwave fields,  $\mathcal{PT}$  symmetry has also been studied experimentally and theoretically in microwave regime utilizing the LRC circuit [20–23], flat microwave cavities (microwave billiard) [51] and circuit QED system [52].

Though conceptually striking, experimental demonstration of  $\mathcal{PT}$  symmetry remains freshly explored in microwave systems. Besides, due to the difficulty of realizing ideal  $\mathcal{PT}$  symmetry abided by the stringent requirement of balanced gain and loss, here we study the  $\mathcal{PT}$ -symmetric-like behavior with non-ideal balance based on the hybrid cavity-magnon system, which works in microwave regime.

The cavity-magnon system [53–71] we consider here, which is attracting increasing attention, consists of a three-dimensional rectangular microwave cavity and a highly polished single-crystal yttrium iron garnet (YIG) sphere inside. Due to its high spin density ( $4.2 \times 10^{21} \text{ cm}^{-3}$ ), the magnon inside the YIG sphere can achieve strong and even ultrastrong coupling to the microwave cavity [61–66]. By dissipation engineering, a non-Markovian interaction dynamics between the magnon and the microwave cavity photon can be achieved, which enables us to build a magnon gradient memory to store information in the magnon dark modes [67]. Moreover, by hybridizing the cavity-magnon system with a superconducting qubit, the coherent strong coupling between magnon and qubit, as a result of the virtual photon mediation, has been demonstrated [68, 69]. The magnetostrictive effect in YIG sphere also provides an alternative mechanism to establish a highly tunable hybrid system, i.e., cavity magnomechanical system [70]. In this case, the YIG sphere hosts the magnon and phonon modes simultaneously, which are coupled to each other through the magnetostrictive interaction. The intrinsic great tunability, low loss and promising integration with other opto- or electromechanical elements make cavity

---

\*Electronic address: liuyulonghs@126.com

†Electronic address: yuxiliu@mail.tsinghua.edu.cn

magnomechanical system also a good candidate to study  $\mathcal{PT}$ -symmetry.

Motivated by the works [32–35] and based on the cavity magnomechanical system [70], we propose to construct a  $\mathcal{PT}$ -symmetric-like system with the passive cavity and active magnon modes. Our proposal is different from previous ones, which introduce gain to microwave cavity photons, either by directly engineering an active microwave cavity [58] or in virtue of the feeding fields by tuning the power ratio and phase difference between different ports [59]. We implement our idea by introducing gain to the magnon mode, in the way of resonantly driving the YIG sphere. In contrast to the blue sideband driving case [72–81], the resonant driving guarantees the stable steady state value of system. Besides, compared to active-cavity-case, the gain of the magnon mode can be easily modulated by the power of the control field without changing the other parameters. The effective gain of the magnon mode, mainly coming from the counter-rotating magnon-phonon interaction terms [80, 81], greatly enhances the fields on the first- and second-order sidebands. Such enhancement can be used to control the amplitude and time delay of the output field. The condition to optimize these abilities will be demonstrated by the response of the system to the power of the control field, magnon-photon coupling strength, and the cavity-waveguide coupling parameters. Particularly, the relation between the  $\mathcal{PT}$ -symmetric-like behavior and the magnon-photon coupling strength will be studied.

The paper is organized as follows. In Sec. II, we introduce the theoretical model of the cavity magnomechanical system and derive the equations of motion for the system variables. In Sec. III, we first study the magnomechanical system, i.e., assume that there is no coupling between the magnon and cavity, to show how the gain of the magnon mode can be achieved by resonantly driving the YIG sphere. Then we study the transmission of the first- and second-order sidebands of the control field for the magnomechanical system. We also show the controllable phase transition in the  $\mathcal{PT}$ -symmetric-like system composed of the passive cavity and active magnon modes. In Sec. IV, we study the influence of the  $\mathcal{PT}$  symmetry on the sideband response of the output field. We demonstrate the tunability between different transmission spectra (amplification or magnomechanically induced absorption) and time delay (positive or negative) on the first-order Stokes sideband. Moreover, the amplification of transmission amplitude and gain-dominated group delay on the second-order Stokes sideband [82] are also shown in Sec. IV. We finally summarize our results in Sec. V. The derivations of the total Hamiltonian are given in Appendix A, while the stability of the system is discussed and shown in Appendix B. The explicit processes for deriving the amplitude of the transmitted field in the total cavity magnomechanical system is shown in Appendix C.

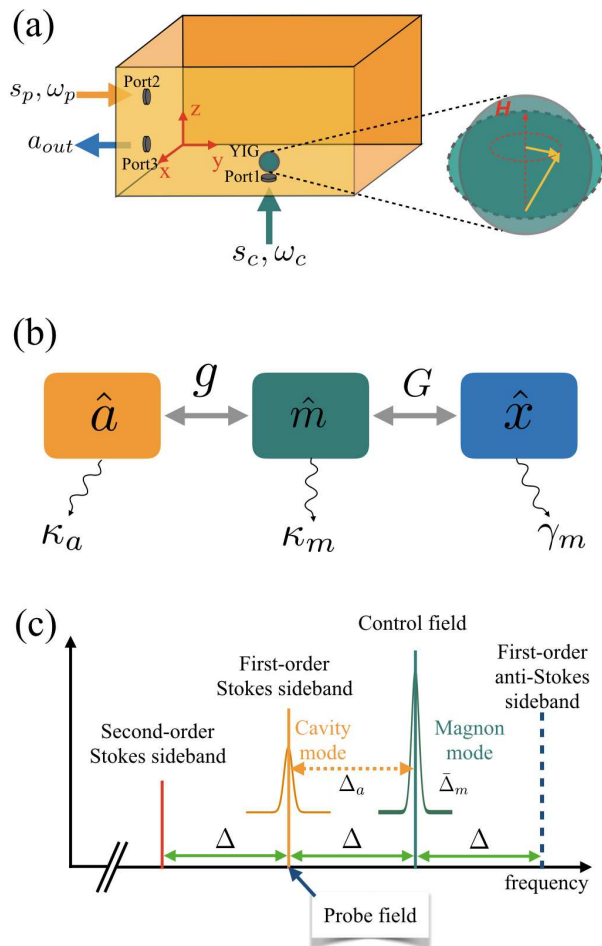


FIG. 1: (Color online) (a) Schematic diagram of the cavity magnomechanical system that consists of a three-dimensional cavity (orange) and a YIG sphere (darkgreen). Usually the YIG sphere is placed near the maximum microwave magnetic field of the cavity mode, and a uniform magnon mode is excited by the uniform external magnetic field ( $H$ ) applied along the  $z$  direction. The ellipse with darkgreen-dashed curve (zoom-in view) denotes the deformation caused by the magnetostrictive force, that is, the mechanical oscillation is produced. A control field with the frequency  $\omega_c$  and amplitude  $s_c$  is applied directly to the YIG sphere via port 1, while a probe field with the frequency  $\omega_p$  and amplitude  $s_p$  is applied through port 2. Port 3 is used for the measurement of transmission. (b) The equivalent coupled-harmonic-resonator model. The parameters  $\kappa_a$ ,  $\kappa_m$  and  $\gamma_m$  denote the decay rates of the microwave cavity, magnon and mechanical resonator modes, respectively. The magnon mode is coupled to the cavity mode with strength  $g$ , while  $G$  is the coupling strength between the magnon and the mechanical resonator. (c) Frequency spectrum of the cavity magnomechanical system. The control field is applied resonantly to the magnon mode, i.e., their effective frequency detuning  $\bar{\Delta}_m = \omega_c - \omega_m - G\bar{x} = 0$ . Here  $\bar{x}$  is the average displacement of the mechanical resonator. The frequency of the cavity mode is detuned from the control field by  $\Delta_a = \omega_c - \omega_a$ . The optical response of the cavity mode is probed by a weak field, whose frequency detuning to the control field is labeled by  $\Delta = \omega_p - \omega_c$ . The first- and second-order sidebands are marked with colorful lines.

## II. THEORETICAL MODEL

### A. Hamiltonian

As schematically shown in Fig. 1(a), we consider a cavity magnomechanical system, consisting of a three-dimensional rectangular microwave cavity and a YIG sphere. The equivalent physical model of this hybrid system is shown in Fig. 1(b). Due to its material and geometrical properties, the YIG sphere, which is placed inside the cavity, hosts the magnon and mechanical modes, simultaneously. As shown in the zoom-in view of the YIG sphere in the right part of Fig. 1(a), a uniform magnon mode with the frequency  $\omega_m = \gamma H$  is excited, when an external magnetic field  $H$  is applied along the  $z$  direction of the rectangular cavity. Here  $\gamma$  is the gyromagnetic ratio. The magnetostrictive effect causes deformation of the spherical geometry and produces mechanical oscillations, which affect the magnon excitation in turn and thus lead to the coupling between the mechanical resonator and the magnon. In our proposal, a control field at frequency  $\omega_c$  with power  $P_c$  is applied directly to the magnon mode, while a weak microwave signal at frequency  $\omega_p$  with power  $P_p$  is used to probe the cavity response. The amplitudes of the control and probe fields are normalized to  $s_c = \sqrt{P_c/\hbar\omega_c}$ ,  $s_p = \sqrt{P_p/\hbar\omega_p}$ , respectively. In the rotating reference frame of the control field at the frequency  $\omega_c$ , the Hamiltonian of the cavity magnomechanical system can be written as

$$\begin{aligned} \mathcal{H} = & -\hbar\Delta_a a^\dagger a - \hbar\Delta_m m^\dagger m + \frac{p^2}{2m_{\text{eff}}} + \frac{1}{2}m_{\text{eff}}\Omega_m^2 x^2 \\ & + \hbar g (am^\dagger + a^\dagger m) + \hbar Gxm^\dagger m \\ & + i\hbar\sqrt{\eta_m\kappa_m} (s_c m^\dagger - s_c^* m) \\ & + i\hbar\sqrt{\eta_a\kappa_a} (s_p e^{-i\Delta t} a^\dagger - s_p^* e^{i\Delta t} a). \end{aligned} \quad (1)$$

Here  $a$  ( $a^\dagger$ ) and  $m$  ( $m^\dagger$ ) are the annihilation (creation) operators of the microwave cavity and magnon modes with resonant frequencies  $\omega_a$  and  $\omega_m$ , respectively. The parameter  $g$  denotes the coupling strength between cavity and magnon modes, which decay at the rates  $\kappa_a$  and  $\kappa_m$ , respectively.  $x$  and  $p$  are the position and momentum operators of the mechanical degree of YIG sphere with effective mass  $m_{\text{eff}}$  and angular frequency  $\Omega_m$ . The mechanical mode in YIG sphere decays at the rate  $\gamma_m$ . The parameter  $G$  denotes the magnon-mechanical coupling strength caused by the magnetostrictive effect. The exact values of the system parameters in our work are referred to relevant experiment in Ref. [70] and located in the microwave regime. Specifically, we use the cavity  $TE_{011}$  mode, which decays at the rate  $\kappa_a/2\pi = 1.675$  MHz and resonates at  $\omega_a/2\pi = 7.86$  GHz. The magnon mode decays at the rate  $\kappa_m/2\pi = 0.56$  MHz, its resonant frequency can be tuned via the bias magnetic field  $H$  and kept in the microwave regime. The mechanical  $S_{1,2,2}$  mode we consider, resonates at frequency  $\Omega_m/2\pi = 11.42$  MHz with the linewidth  $2\gamma_m = 300$  Hz, and is coupled

to the magnon mode with the strength  $G = 9.88$  mHz.

Besides, the frequency spectrum of the total cavity magnomechanical system is shown in Fig. 1(c). The frequency detunings of the cavity and magnon modes to the control field are labeled as  $\Delta_a = \omega_c - \omega_a$  and  $\Delta_m = \omega_c - \omega_m$ , respectively, while the detuning of the probe field from the control field is  $\Delta = \omega_p - \omega_c$ . The first- and second-order sidebands located at  $\omega_c + \Delta$ ,  $\omega_c - \Delta$  and  $\omega_c - 2\Delta$  are labeled as blue-dashed, orange-solid and red-solid curves in Fig. 1(c). The lower sidebands respect to the control field, resulting from the down-conversion processes, are regarded as Stokes sidebands, while the upper ones, resulting from the up-conversion processes, are referred to as anti-Stokes sidebands. Moreover, the coefficient  $\eta_a$  ( $\eta_m$ ) represents the coupling parameter between the waveguide and the cavity (YIG sphere). Furthermore, we classify the coupling parameter  $\eta_a$  into three categories [83], i.e., over coupling ( $\eta_a > 1/2$ ), critical coupling ( $\eta_a = 1/2$ ) and under coupling ( $\eta_a < 1/2$ ).

### B. Equations of motion

The dynamics of the total cavity magnomechanical system can be described by solving the Heisenberg-Langevin equations [84]

$$\begin{aligned} \dot{a} = & \left(i\Delta_a - \frac{\kappa_a}{2}\right)a - igm + \sqrt{\eta_a\kappa_a}s_p e^{-i\Delta t} \\ & + \sqrt{(1-\eta_a)\kappa_a}\Gamma_a(t), \end{aligned} \quad (2)$$

$$\begin{aligned} \dot{m} = & \left(i\Delta_m - \frac{\kappa_m}{2}\right)m - iGxm - iga \\ & + \sqrt{\eta_m\kappa_m}s_c + \sqrt{(1-\eta_m)\kappa_m}\Gamma_m(t), \end{aligned} \quad (3)$$

$$\dot{x} = \frac{p}{m_{\text{eff}}}, \quad (4)$$

$$\dot{p} = -m_{\text{eff}}\Omega_m^2 x - \hbar Gm^\dagger m - \gamma_m p + \xi(t). \quad (5)$$

Here  $\Gamma_a(t)$ ,  $\Gamma_m(t)$ , and  $\xi(t)$  represent the fluctuation operators corresponding to the cavity, magnon and mechanical resonator, respectively. All the fluctuation operators have zero means, i.e.,

$$\langle \Gamma_a(t) \rangle = 0, \quad (6)$$

$$\langle \Gamma_m(t) \rangle = 0, \quad (7)$$

$$\langle \xi(t) \rangle = 0. \quad (8)$$

Here the averages are made over the equilibrium state of the environment. The correlation functions of the fluctuation operators of the cavity and magnon modes, i.e.,  $\Gamma_a(t)$  and  $\Gamma_m(t)$ , with their Hermitian conjugates, satisfy the conditions

$$\langle \Gamma_a(t)\Gamma_a^\dagger(t') \rangle = \kappa_a \delta(t-t'), \quad (9)$$

$$\langle \Gamma_m(t)\Gamma_m^\dagger(t') \rangle = \kappa_m \delta(t-t'), \quad (10)$$

in the time domain under the Markovian approximation. The thermal energy due to the cryogenic environment with the temperature  $T$ , e.g., 22 mK in Ref. [85],

is much lower than the eigenenergies of the cavity and magnon modes, which are several gigahertz in the microwave regime. That is,  $k_B T \ll \hbar\omega_a, \hbar\omega_m$ . In this case, it is reasonable to neglect the effects of the environmental temperature on the cavity and magnon modes. Here  $k_B$  is the Boltzmann constant. However, the frequency of the mechanical resonator is usually several megahertz and much smaller than the frequencies of cavity and magnon modes. Therefore, the temperature effect on the mechanical resonator should be taken into account. The thermal Langevin force  $\xi(t)$ , acting on the mechanical resonator, has the nonzero correlation [86, 87]

$$\langle \xi(t)\xi(t') \rangle = \frac{1}{2\pi} \int \exp[-i\omega(t-t')] N(\omega) d\omega. \quad (11)$$

Here  $N(\omega)$  represents the thermal phonon number of the mechanical resonator, and is given as

$$N(\omega) = \hbar\gamma_m m_{\text{eff}} \omega \left[ 1 + \coth \left( \frac{\hbar\omega}{2k_B T} \right) \right]. \quad (12)$$

Since we are interested in the mean response of the system to the probe field, it is reasonable to focus on the expectation values of the operators. Thus, the semiclassical equations of motion can be derived from Eqs. (2-5) as

$$\frac{d\langle a \rangle}{dt} = \left( i\Delta_a - \frac{\kappa_a}{2} \right) \langle a \rangle - ig\langle m \rangle + \sqrt{\eta_a \kappa_a} s_p e^{-i\Delta t} \quad (13)$$

$$\frac{d\langle m \rangle}{dt} = \left( i\Delta_m - \frac{\kappa_m}{2} \right) \langle m \rangle - iG\langle x \rangle \langle m \rangle - ig\langle a \rangle + \sqrt{\eta_m \kappa_m} s_c, \quad (14)$$

$$\frac{d\langle x \rangle}{dt} = \frac{\langle p \rangle}{m_{\text{eff}}}, \quad (15)$$

$$\frac{d\langle p \rangle}{dt} = -m_{\text{eff}} \Omega_m^2 \langle x \rangle - \hbar G \langle m^\dagger \rangle \langle m \rangle - \gamma_m \langle p \rangle. \quad (16)$$

Note that we have used the zero mean values for all fluctuation operators shown in Eqs. (6-8) and mean field approximation, i.e.,  $\langle o_1 o_2 \rangle = \langle o_1 \rangle \langle o_2 \rangle$ . Here  $o_1, o_2$  can be any system operators.

### III. GAIN AND PT-SYMMETRIC-LIKE SYSTEM

Before we study the response of the whole cavity magnomechanical system, we would like to focus on the bare magnomechanical system and show the gain mechanism of the magnon first, which lays the foundation for the formation of the  $\mathcal{PT}$ -symmetric-like system. Here, the bare magnomechanical system is referred to the case when the coupling between the cavity and magnon modes is neglected in Eq. (1). Besides, for the bare magnomechanical system, we assume that a probe field with frequency  $\omega'_p$  is applied to detect the response and verify the gain of the magnon mode. The coupling strength between the probe

field and the magnon is  $\sqrt{\eta_m \kappa_m} s'_p$ . Note here the parameters  $s'_p, \omega'_p$  are introduced to discriminate the probe field applied to the magnon with the one applied to the cavity mode, whose amplitude and frequency are labeled by  $s_p$  and  $\omega_p$ , respectively. Taking all these aspects into account, the Hamiltonian of the bare magnomechanical system can be written as

$$\mathcal{H}' = -\hbar\Delta_m m^\dagger m + \frac{p^2}{2m_{\text{eff}}} + \frac{1}{2} m_{\text{eff}} \Omega_m^2 x^2 + \hbar G x m^\dagger m + i\hbar\sqrt{\eta_m \kappa_m} \left[ (s_c + s'_p e^{-i\Delta' t}) m^\dagger - h.c. \right], \quad (17)$$

where  $\Delta' = \omega'_p - \omega_c$  represents the detuning between the probe and control fields applied to the magnon mode.

In this case, following the same processes in Sec. II B, i.e., by solving the Heisenberg-Langevin equations and taking the averages, we can obtain the semiclassical equations of motion for all the operators in bare magnomechanical system. We note that the equations of motion for the mechanical resonator can still be described by Eqs. (15) and (16), while the equation of motion for the magnon mode in Eq. (14) is modified to

$$\frac{d\langle m \rangle}{dt} = \left( i\Delta_m - \frac{\kappa_m}{2} \right) \langle m \rangle - iG\langle x \rangle \langle m \rangle + \sqrt{\eta_m \kappa_m} (s_c + s'_p e^{-i\Delta' t}). \quad (18)$$

The nonlinear equations of motion for the bare magnomechanical system, as shown in Eqs. (15), (16) and (18), cannot be solved precisely since their steady-state solutions have infinite number of frequencies. To approximately obtain the steady-state solutions which are exact for the strong driving  $s_c$  and corrected to the second order for the weak probe  $s'_p$ , we can apply the perturbation theory and make the following ansatz

$$\langle m \rangle = \bar{m} + \langle \delta m \rangle, \quad \langle x \rangle = \bar{x} + \langle \delta x \rangle, \quad (19)$$

with  $|\bar{m}| \gg |\delta m|$  and  $|\bar{x}| \gg |\delta x|$ , respectively [83, 88–90]. Here  $\bar{m}$  and  $\bar{x}$  are exact steady state values of the system when  $s'_p = 0$ , while  $\langle \delta m \rangle$  and  $\langle \delta x \rangle$  are the small quantities around the steady-state values and proportional to the probe field  $s'_p$ . Substituting these ansatzes into Eqs. (15), (16) and (18), we can obtain the steady-state values  $\bar{m}$  and  $\bar{x}$  of the magnon and mechanical resonator modes as

$$\bar{m} = -\frac{2\sqrt{\eta_m \kappa_m} s_c}{2i\bar{\Delta}_m - \kappa_m}, \quad (20)$$

$$\bar{x} = -\frac{\hbar G |\bar{m}|^2}{m_{\text{eff}} \Omega_m^2}, \quad (21)$$

with the modified detuning  $\bar{\Delta}_m = \Delta_m - G\bar{x}$ . Besides, we can also obtain the equations of motion for the small quantities  $\delta m$  and  $\delta x$  as [83, 88–91]

$$\frac{d\langle \delta m \rangle}{dt} = \left( i\bar{\Delta}_m - \frac{\kappa_m}{2} \right) \langle \delta m \rangle - iG(\bar{m}\langle \delta x \rangle + \langle \delta m \rangle \langle \delta x \rangle) + \sqrt{\eta_m \kappa_m} s'_p e^{-i\Delta' t}, \quad (22)$$

$$\mathcal{D}\langle \delta x \rangle = -\frac{\hbar G}{m_{\text{eff}}} [\bar{m} (\langle \delta m^\dagger \rangle + \langle \delta m \rangle) + \langle \delta m^\dagger \rangle \langle \delta m \rangle] \quad (23)$$

with  $\mathcal{D} = \frac{d^2}{dt^2} + \Omega_m^2 + \gamma_m \frac{d}{dt}$  denoting the differential operation related to the mechanical resonator. The nonlinear terms  $-iG\langle\delta m\rangle\langle\delta x\rangle$  and  $-\hbar G\langle\delta m^\dagger\rangle\langle\delta m\rangle$  in Eqs. (22) and (23) will surely induce several higher sidebands corresponding to the control field. In other parts of our work, we mainly focus on the first- and second-order sidebands.

### A. Spectrum of the transmitted field

To obtain the solutions of  $\langle\delta m\rangle$  and  $\langle\delta x\rangle$ , which are described by the nonlinear equations in Eqs. (22) and (23), we make the ansatz up to the second-order sideband for a given detuning  $\Delta'$  as follows

$$\langle\delta m\rangle = m_1^- e^{-i\Delta't} + m_1^+ e^{i\Delta't} + m_2^- e^{-i2\Delta't} + m_2^+ e^{2i\Delta't}, \quad (24)$$

$$\langle\delta m^*\rangle = (m_1^+)^* e^{-i\Delta't} + (m_1^-)^* e^{i\Delta't} + (m_2^+)^* e^{-i2\Delta't} + (m_2^-)^* e^{2i\Delta't}, \quad (25)$$

$$\langle\delta x\rangle = x_1 e^{-i\Delta't} + x_1^* e^{i\Delta't} + x_2 e^{-2i\Delta't} + x_2^* e^{2i\Delta't} \quad (26)$$

Here we have neglected the higher-order sidebands with the frequencies  $n\Delta'$  ( $n \geq 3$ ). Substituting Eqs. (24-26) into Eqs. (22) and (23), comparing the frequency terms, we obtain a set of coupled equations about different frequency components. For the first-order response of the probe field, i.e., terms with  $e^{\pm i\Delta't}$ , we have

$$\lambda_m(\Delta') m_1^- = -iG\bar{m}x_1 + \sqrt{\eta_m \kappa_m} s_p, \quad (27)$$

$$\lambda_m^\dagger(\Delta') m_1^+ = iG\bar{m}x_1^*, \quad (28)$$

$$\chi^{-1}(\Delta') x_1 = -\hbar G [\bar{m}^* m_1^- + \bar{m}(m_1^+)^*], \quad (29)$$

with

$$\lambda_m(\Delta') = -i(\bar{\Delta}_m + \Delta') + \frac{\kappa_m}{2}, \quad (30)$$

$$\chi(\Delta') = [m_{\text{eff}}(\Omega_m^2 - \Delta'^2 - i\Delta'\gamma_m)]^{-1}, \quad (31)$$

representing the magnon response function and mechanical susceptibility, respectively. Note that we have neglected the small influences of the second-order sidebands, i.e., terms with  $e^{\pm 2i\Delta't}$ , whose amplitudes are much smaller than the probe field. Besides, we define

$$\lambda_m^\dagger(\Delta') = [\lambda_m(-\Delta')]^*. \quad (32)$$

Then the coefficients of the first-order Stokes sideband, i.e., the solutions of the coupled equations in Eqs. (27-29), can be obtained as

$$m_1^- = \frac{1 + if(\Delta')}{\lambda_m(\Delta') + 2\bar{\Delta}_m f(\Delta')} \sqrt{\eta_m \kappa_m} s_p', \quad (33)$$

$$x_1 = \frac{-\hbar G \bar{m} \chi(\Delta')}{\lambda_m(\Delta') + 2\bar{\Delta}_m f(\Delta')} \sqrt{\eta_m \kappa_m} s_p', \quad (34)$$

with

$$f(\Delta') = \hbar G^2 \bar{m}^2 \chi(\Delta') [\lambda_m^\dagger(\Delta')]^{-1}. \quad (35)$$

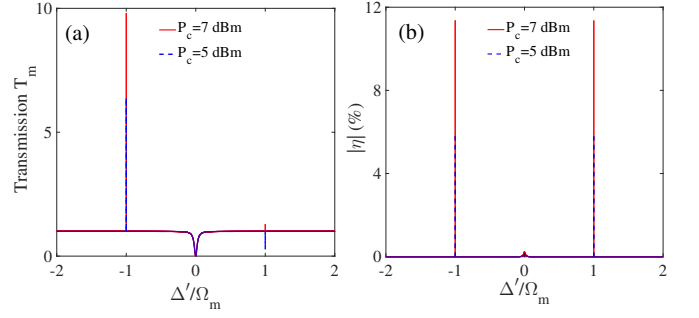


FIG. 2: (Color online) (a) Transmission coefficient  $T_m$  on the first-order sideband and (b) the amplitude  $|\eta|$  on the second-order sideband versus the probe and control field detuning  $\Delta'$ , for the bare magnomechanical system under different powers of control field, e.g.,  $P_c = 5$  dBm (red-dashed line) and  $P_c = 7$  dBm (blue-solid line). The coupling parameter  $\eta_m = 0.5$ .

Similarly, we can also obtain equations concerning the coefficients of the terms with  $e^{\pm 2i\Delta't}$  as follows:

$$\lambda_m(2\Delta') m_2^- = -iG m_1^- x_1 - iG \bar{m} x_2, \quad (36)$$

$$\lambda_m^\dagger(2\Delta') (m_2^+)^* = iG (m_1^+)^* x_1 + iG \bar{m}^* x_2, \quad (37)$$

$$\chi^{-1}(2\Delta') x_2 = -\hbar G [\bar{m}^* m_2^- + \bar{m} (m_2^+)^* + (m_1^+)^* m_1^-]. \quad (38)$$

Then, the amplitude of the second-order Stokes sideband, i.e.,  $m_2^-$ , can be obtained as

$$m_2^- = \frac{iG^2 \bar{m} f^{(2)}(\Delta') x_1^2 - iG [1 + \Delta' f^{(2)}(\Delta')] m_1^- x_1}{\lambda_m(2\Delta') + 2\bar{\Delta}_m f(2\Delta')}, \quad (39)$$

with

$$f^{(2)}(\Delta') = -f(2\Delta') [\lambda_m^\dagger(\Delta')]^{-1}. \quad (40)$$

The two terms in the numerator of the right hand side of Eq. (39) actually denote two processes. The first term with  $x_1^2$  stems from the two-phonon down-conversion directly from the control field, i.e., the direct second-order sideband. The second term with  $m_1^- x_1$  originates from the down-conversion of the first-order Stokes sideband, i.e., indirect second-order sideband [88–90].

According to the input-output theory [92], the response of the bare magnomechanical system can be detected by the expectation of the output field, which can be given as

$$\langle s'_{out} \rangle = s_c + s_p' e^{-i\Delta't} - \sqrt{\eta_m \kappa_m} \langle m \rangle. \quad (41)$$

Substituting Eqs. (19), (20), and (24) into Eq. (41), we can obtain the mean value of the output field as follows:

$$\langle s'_{out} \rangle = s_c - \sqrt{\eta_m \kappa_m} \bar{m} + (s_p' - \sqrt{\eta_m \kappa_m} m_1^-) e^{-i\Delta't} - \sqrt{\eta_m \kappa_m} (m_1^+ e^{i\Delta't} + m_2^- e^{-2i\Delta't} + m_2^+ e^{2i\Delta't}). \quad (42)$$

The amplitude of the rescaled transmission field at the frequency of the probe field, i.e.,  $\omega_p$ , can be formulated as

$$\begin{aligned} t_p^m &= \frac{s'_p - \sqrt{\eta_m \kappa_m} m_-}{s'_p} \\ &= 1 - \frac{1 + if(\Delta')}{\lambda_m(\Delta') + 2\bar{\Delta}_m f(\Delta')} \eta_m \kappa_m. \end{aligned} \quad (43)$$

Then the power transmission coefficient  $T_m = |t_p^m|^2$  can be given correspondingly. The stability of the system is checked carefully by the Routh-Hurwitz criterion [93] for all the parameters we used, and is demonstrated in Appendix B.

In our study, we focus on the resonant driving case, i.e.,  $\bar{\Delta}_m = 0$ . Then the power transmission at the first-order Stokes and anti-Stokes sidebands can be further expressed as

$$T_m(-\Omega_m) \simeq \left(1 + \frac{y}{2\mu}\right)^2, \quad (44)$$

$$T_m(\Omega_m) \simeq \left(1 - \frac{y}{2\mu}\right)^2, \quad (45)$$

with

$$\mu = \Omega_m / \kappa_m, \quad y = -\text{Re}[f(-\Omega_m)]. \quad (46)$$

Here,  $f(-\Omega_m)$  is obtained by replacing  $\Delta'$  with  $-\Omega_m$  in Eq. (35). Thus, it is obviously that the rescaled power of the transmission field at the Stokes sideband  $T_m(-\Omega_m)$  is always larger than 1, while for the anti-Stokes sideband, only when the power of the control field surpasses the threshold

$$P_{\text{thr}} = \frac{\Omega_m \omega_1 m_{\text{eff}} \gamma_m}{\eta_m G^2} \left( \Omega_m^2 + \frac{\kappa_m^2}{4} \right), \quad (47)$$

can the rescaled power of transmission field  $T_m(\Omega_m)$  exceed 1.

In Fig. 2(a), we show the response of the bare magnomechanical system for two configurations, i.e., when the power  $P_c$  of the control field is below or above the threshold  $P_{\text{thr}}$ . For the parameters used in our study, the threshold pump power  $P_{\text{thr}}$  is 6.6 dBm. Being consistent with Eqs. (44) and (45), we find great amplification on the first-order Stokes sideband. When the rescaled control field power  $P_c$  is increased from 5 dBm (blue-dashed line) to 7 dBm (red-solid line), the rescaled transmission coefficient  $T_m$  is increased from 6.357 to 9.797 on the Stokes sideband, while from 0.274 to 1.280 on the anti-Stokes sideband. Actually, the amplification can be attributed to the effective gain on the first-order sideband, whose mechanism will be discussed in Sec. III B.

Moreover, the amplitude of the output field on the second-order Stokes sideband can be renormalized as

$$|\eta| = \left| \frac{\sqrt{\eta_m \kappa_m} m_2^-}{s'_p} \right|. \quad (48)$$

In Fig. 2(b),  $|\eta|$  is shown as a function of the detuning  $\Delta'$ , i.e., the frequency difference between the probe and control fields, under the given powers  $P_c = 5$  dBm (blue-dashed line) and 7 dBm (red-solid line) of the control field, respectively. The rescaled amplitude  $|\eta|$  of the second-order sideband behaves symmetrically at the detuning  $\Delta' = \pm\Omega_m$  as a result of resonantly driving. We observe an increment of 5.556% from 5.794% at 5 dBm to 11.350% at 7 dBm. We find that the amplitude of the second-order sideband mainly comes from the contribution of the down-conversion induced by the first-order sideband, i.e., the terms with  $m_1^- x_1$  in Eq. (39). Thus, it is reasonable that the amplitude of the second-order sideband can also be amplified by the effective gain on the first-order sideband.

### B. Effective gain in magnon on the first-order Stokes sideband

We now further study the gain mechanism of the magnon mode. We first consider Eqs. (22) and (23) without the probe field, i.e.,  $s'_p = 0$ . In this case, with the Fourier transform, Eqs. (22) and (23) can be reexpressed as

$$\begin{aligned} \lambda_m(\omega) \langle \delta m(\omega) \rangle &= -iG \langle \delta m(\omega) \rangle * \langle \delta x(\omega) \rangle \\ &\quad - iG \bar{m} \langle \delta x(\omega) \rangle \end{aligned} \quad (49)$$

$$\begin{aligned} \chi^{-1}(\omega) \langle \delta x(\omega) \rangle &= -\hbar G \bar{m} [\langle \delta m^\dagger(\omega) \rangle + \langle \delta m(\omega) \rangle] \\ &\quad - \hbar G \langle \delta m^\dagger(\omega) \rangle * \langle \delta m(\omega) \rangle. \end{aligned} \quad (50)$$

Here  $\delta m(\omega)$  and  $\delta x(\omega)$  represent the Fourier transforms of the magnon and mechanical modes, respectively. The functions  $\lambda_m(\omega)$  and  $\chi(\omega)$  can be obtained by replacing  $\Delta'$  with  $\omega$  in Eqs. (30) and (31). Terms in the form of  $h_1 * h_2$ , which denote the convolution of two functions  $h_1$  and  $h_2$ , can be expressed as [94]

$$h_1 * h_2 = \int_{-\infty}^{+\infty} d\omega_1 h_1(\omega_1) h_2(\omega - \omega_1). \quad (51)$$

Substituting Eq. (50) into Eq. (49) and only retaining the linear and quadratic terms, we can rewrite Eq. (49) as

$$\left[ -i(\bar{\Delta}'_m + \omega) + \frac{\kappa'_m}{2} \right] \langle \delta m(\omega) \rangle = -iG' [\langle \delta m(\omega) \rangle * \langle \delta x(\omega) \rangle], \quad (52)$$

with

$$\bar{\Delta}'_m = \bar{\Delta}_m + \text{Im}[r^{-1}(\omega)], \quad (53)$$

$$\kappa'_m = \kappa_m - 2\text{Re}[r^{-1}(\omega)], \quad (54)$$

denoting the modified detuning and decay rate of magnon mode, respectively. Here,  $r(\omega)$  is defined as

$$r(\omega) = [\lambda_m^\dagger(\omega)]^{-1} - i[\hbar\chi(\omega)G^2\bar{m}^2]^{-1} = U + iV. \quad (55)$$

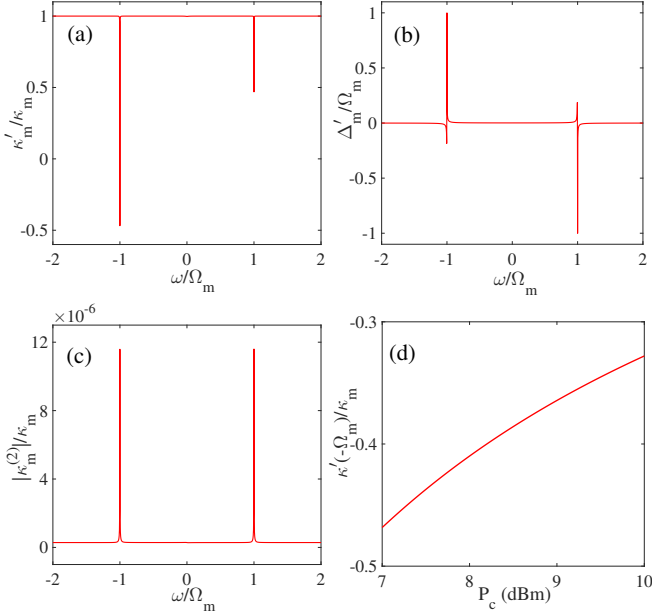


FIG. 3: (Color online) Spectra of the effective decay rate  $\kappa'_m$ , effective detuning  $\bar{\Delta}'_m$  and the amplification coefficient  $\kappa_m^{(2)}$  under the specific power of control field  $P_c = 7$  dBm, are shown in (a), (b) and (c), respectively. (d) shows the effective decay rate on the first-order Stokes sideband  $\kappa'_m(-\Omega_m)$  versus the control field power  $P_c$ . Other parameters are the same as Fig. 2.

The parameters  $U$  and  $V$ , representing the real and imaginary parts of  $r(\omega)$ , can be expressed explicitly as

$$U = -\frac{m_{\text{eff}}\omega\gamma_m}{\hbar G^2 \bar{m}^2} + \frac{2\kappa_m}{4(\bar{\Delta}'_m - \omega)^2 + \kappa_m^2}, \quad (56)$$

$$V = -\frac{m_{\text{eff}}(\Omega_m^2 - \omega^2)}{\hbar G^2 \bar{m}^2} - \frac{4(\bar{\Delta}'_m - \omega)}{4(\bar{\Delta}'_m - \omega)^2 + \kappa_m^2}. \quad (57)$$

It is obvious that the magnon mode can be amplified when  $\kappa'_m < 0$ , i.e., the magnon mode can obtain the gain. Moreover, the parameter  $G' = \kappa_m^{(2)}G$ , with

$$\kappa_m^{(2)} = 1 + \frac{if(\omega)\lambda_m(\omega)}{1 + if(\omega)} \left\{ [\lambda_m^\dagger(\omega)]^{-1} - [\lambda_m(0)]^{-1} \right\}, \quad (58)$$

denoting the gain-induced effective amplification coefficient on the second-order interaction. Here the function  $f(\omega)$  can be obtained by replacing  $\Delta'$  with  $\omega$  in Eq. (35).

In Figs. 3(a) and 3(b), we show the variations of the effective dissipation rate  $\kappa'_m$  and detuning  $\bar{\Delta}'_m$  of the magnon mode with rescaled  $\omega$ , under a given power  $P_c = 7$  dBm of the control field. We can find that the normalized effective dissipation rate  $\kappa'_m/\kappa_m$  takes a negative value on the first-order Stokes sideband, i.e.,  $\kappa'_m(-\Omega_m) < 0$ , which corresponds to an effective gain. Meanwhile, the effective detuning on the first-order Stokes sideband  $\bar{\Delta}'_m(-\Omega_m)$  is changed from the 0 to  $\Omega_m$ , resulting the resonance with the cavity mode, whose effect will be

taken into account in Sec. III C. The negative decay rate  $\kappa'_m(-\Omega_m)$  and resonant condition  $\bar{\Delta}'_m(-\Omega_m) = \Delta_a = \Omega_m$  lay the foundation of  $\mathcal{PT}$ -symmetric-like behavior of the cavity magnomechanical system, which we will show in Sec. III C.

Besides, the gain-induced amplification coefficient  $|\kappa_m^{(2)}|$  on the second-order conversion process is shown in Fig. 3(c). We find symmetric amplification on the Stokes- and anti-Stokes sidebands as a result of resonant driving. This shows consistency with the symmetric amplitude  $|\eta|$  in Fig. 2(b). The amplification on the second-order sideband mainly originates from the gain-induced enhancement of the down-conversion process of the first-order sideband, which gets negative dissipation rate as shown in Fig. 3(a). Moreover, in Fig. 3(d), we show the influence of the control field power  $P_c$  on the effective decay rate  $\kappa'_m(-\Omega_m)$  of the first-order Stokes sideband. We find that the negative decay rate  $\kappa'_m(-\Omega_m)$  becomes larger with the increase of the power  $P_c$ , i.e., the effective gain  $-\kappa'_m(-\Omega_m)$  becomes smaller, which can be inferred from Eqs. (20), (54) and (56). Actually, the decrease of the gain can be attributed to the increase of the decay from the mechanical resonator as shown in Fig. 1(b), as a result of the stronger effective coupling  $G\bar{m}$  induced by higher control field power.

We have shown the gain mechanism of the magnon mode on the first-order sideband. Considering the rigidity to realize amplification and gain on the first-order anti-Stokes sideband, as shown in Eq. (47) and Fig. 3(a), we mainly focus on the amplification on the first-order Stokes sideband in the rest of our paper. Besides, we note that the spectra of the effective detuning  $\bar{\Delta}'_m$  and decay rate  $\kappa'_m$  are centered around  $-\Omega_m$ , thus it is reasonable to conduct the Weisskopf-wigner approximation [84]. Then, we can obtain an active magnon mode, with the effective gain  $-\kappa'_m(-\Omega_m)$  and effective detuning  $\bar{\Delta}'_m(-\Omega_m)$  to the control field. This active magnon mode, which is introduced by resonantly driving the YIG sphere, provides us the possibility to construct a  $\mathcal{PT}$ -symmetric-like system with the passive microwave cavity mode.

### C. Controllable phase transition

Let us now include the microwave cavity mode and consider the full Hamiltonian shown in Eq. (1). We assume that the microwave cavity field is coupled resonantly to the first-order Stokes sideband of the control field, i.e.,  $\Delta_a = \Omega_m$ . When the cavity mode is included, we find the response function of the magnon mode is modified from  $\lambda_m(\omega)$  to  $\lambda_m(\omega) + g^2/\lambda_a(\omega)$ . The effective detuning  $\bar{\Delta}'_m$  in Eq. (53), decay rate  $\kappa'_m$  in Eq. (54), and effective amplification coefficient  $\kappa_m^{(2)}$  in Eq. (58) are also modified correspondingly, by replacing  $\lambda_m(\omega)$  with  $\lambda_m(\omega) + g^2/\lambda_a(\omega)$ . However, due to the negligibly small influence of  $g^2/\lambda_a(\omega)$  on the effective gain and detuning, it is reasonable to neglect the back-action of the cavity to

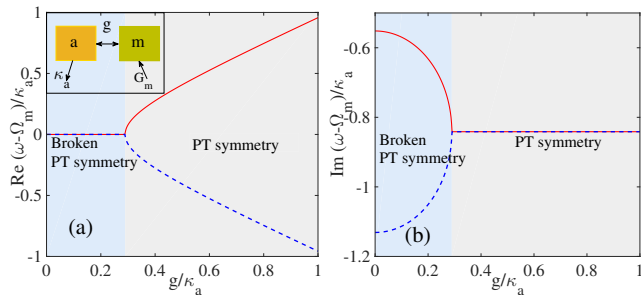


FIG. 4: (Color online) The equivalent  $\mathcal{PT}$ -symmetric-like coupled cavity and magnon model with effective loss  $\kappa_a$  and gain  $G_m$  is embedded in (a). The real and imaginary parts of the eigenfrequencies  $\omega_+$  and  $\omega_-$  versus the magnon-photon coupling strength  $g$  are plotted in (a) and (b), with red-solid and blue-dotted curves, respectively. Light blue and gray patches are used to label the broken and unbroken  $\mathcal{PT}$ -symmetric phases, respectively. Other parameters are  $\tilde{\Delta}_m = \Delta_a = \Omega_m$  and  $G_m = 0.1586 \kappa_a$ .

the magnon mode here. In this case, we construct a  $\mathcal{PT}$ -symmetric-like system as shown in the inset of Fig. 4(a), based on the coupled cavity-magnon system. The passive microwave cavity mode, which decays at the rate  $\kappa_a$ , is coupled resonantly to the effective active magnon mode, whose effective gain is  $G_m = -\kappa'_m(-\Omega_m)$ , with the strength  $g$ .

The effective non-Hermitian Hamiltonian of the coupled cavity-magnon system with the effective gain and loss can be written as

$$\mathcal{H}_{\text{eff}} = \left( \tilde{\Delta}_m + i\frac{G_m}{2} \right) \delta m^\dagger \delta m + \left( \Delta_a - i\frac{\kappa_a}{2} \right) \delta a^\dagger \delta a + g (\delta m^\dagger \delta a + \delta a^\dagger \delta m), \quad (59)$$

with  $\tilde{\Delta}_m = \tilde{\Delta}'_m(-\Omega_m)$  denoting the effective detuning between the active magnon mode and the control field. The coupling of the magnon and cavity modes leads to two supermodes, i.e.,  $D_+ = (\delta m + \delta a)/\sqrt{2}$  and  $D_- = (\delta m - \delta a)/\sqrt{2}$ , with the corresponding eigenfrequencies

$$\omega_{\pm} = \frac{1}{2} \left( \tilde{\Delta}_m + \Delta_a \right) - \frac{i}{4} (\kappa_a - G_m) \pm \sqrt{g^2 - \left[ -\frac{i}{2} (\tilde{\Delta}_m - \Delta_a) - \frac{1}{4} (G_m + \kappa_a) \right]^2}. \quad (60)$$

Based on the resonant condition  $\tilde{\Delta}_m = \Delta_a = \Omega_m$  which has been shown in Fig. 3(b), the responses of the real and imaginary parts of the eigenfrequencies to the magnon-photon coupling strength  $g$  are shown in Figs. 4(a) and 4(b), respectively. For the parameters used in our study, the effective gain can be obtained as  $G_m = 0.1586 \kappa_a$ . We find that the two supermodes degenerate at the frequency  $\Omega_m$  but have different linewidths  $-(\kappa_a - G_m)/4 \pm \sqrt{(G_m + \kappa_a)^2/16 - g^2}$

when  $g < (\kappa_a + G_m)/4$ , while they decay in the same rates  $(\kappa_a - G_m)/4$  but have different frequencies  $\Omega_m \pm \sqrt{g^2 - (G_m + \kappa_a)^2/16}$  when  $g > (\kappa_a + G_m)/4$ . Actually, the critical point, i.e.,  $(\kappa_a + G_m)/4$ , represents the  $\mathcal{PT}$  phase transition point or the exceptional point (EP) [1, 16, 17, 29, 32, 42, 95, 96]. The regions in which  $g$  is smaller and larger than the critical value correspond to the broken and unbroken  $\mathcal{PT}$ -symmetric spaces, respectively. The phase transition between these two regions can be realized by modulating the magnon-photon coupling strength  $g$ .

#### IV. ENHANCED OUTPUT EFFECTS ON THE FIRST- AND SECOND- ORDER SIDEBANDS

In this section, we will study the output field of the cavity magnomechanical system. In particular, we will show how the  $\mathcal{PT}$  symmetry parameters affect the transmission properties on the first- and second-order sidebands.

##### A. Properties of the transmitted field

In order to give more explicit descriptions of the output fields on both the first- and second-order sidebands, we turn back to the full Hamiltonian of the whole system shown in Eq. (1) in this subsection. Here, we assume that the probe field is applied to the photon mode for studying the response of the cavity magnomechanical system.

The equations of motion for system variables have been given in Eqs. (13–16). Following the same procedure as in Sec. III, we assume that each variable can be written as the sum of the steady-state value and the small quantity around it, e.g.,  $a = \bar{a} + \delta a$  for the cavity mode. Then the steady-state values of the cavity, magnon modes and mechanical resonator can be obtained as

$$\bar{a} = \frac{2ig}{i2\Delta_a - \kappa_a} \bar{m}, \quad (61)$$

$$\bar{m} = \frac{2\sqrt{\eta_m \kappa_m} s_{in}}{-i2\tilde{\Delta}_m + \kappa_m + 2\Gamma'_a}, \quad (62)$$

$$\bar{x} = -\frac{\hbar G |\bar{m}|^2}{m_{\text{eff}} \Omega_m^2}, \quad (63)$$

when the probe field is not applied. Here

$$\Gamma'_a = -\frac{2g^2}{i2\Delta_a - \kappa_a}. \quad (64)$$

The equations of motion for the small quantities around the steady-state values, proportional to the probe field, can be given by

$$\frac{d}{dt} \langle \delta a \rangle = \left( i\Delta_a - \frac{\kappa_a}{2} \right) \langle \delta a \rangle - ig \langle \delta m \rangle + \sqrt{\eta_a \kappa_a} s_p e^{-i\Delta t}, \quad (65)$$

$$\frac{d}{dt}\langle\delta m\rangle = \left(i\bar{\Delta}_m - \frac{\kappa_m}{2}\right)\langle\delta m\rangle - iG(\bar{m}\langle\delta x\rangle - \langle\delta m\rangle\langle\delta x\rangle) - ig\langle\delta a\rangle, \quad (66)$$

$$\mathcal{D}\langle\delta x\rangle = -\frac{\hbar G}{m_{\text{eff}}}\left[\bar{m}(\langle\delta m^\dagger\rangle + \langle\delta m\rangle) + \langle\delta m^\dagger\rangle\langle\delta m\rangle\right] \quad (67)$$

The details of solving these coupled differential equations are shown in Appendix C. Then in terms of the input-output theory [92], we can obtain the mean value of the output field as follows:

$$\begin{aligned} \langle s_{\text{out}}\rangle &= s_p e^{-i\Delta t} - \sqrt{\eta_a \kappa_a} \langle a\rangle, \\ &= -\sqrt{\eta_a \kappa_a} \bar{a} + (s_p - \sqrt{\eta_a \kappa_a} A_1^-) e^{-i\Delta t} \\ &\quad - \sqrt{\eta_a \kappa_a} A_1^+ e^{i\Delta t} - \sqrt{\eta_a \kappa_a} (A_2^- e^{-2i\Delta t} + A_2^+ e^{2i\Delta t}). \end{aligned} \quad (68)$$

The corresponding amplitudes of the rescaled output field on the first- and second-order Stokes sidebands read

$$t_p = \frac{s_p - \sqrt{\eta_a \kappa_a} A_1^-}{s_p} = 1 - \eta_a \kappa_a F(\Delta), \quad (69)$$

$$|\eta'| = \left| \frac{\sqrt{\eta_a \kappa_a} A_2^-}{s_p} \right|, \quad (70)$$

respectively. The explicit expressions of the parameters  $A_1^\pm$ ,  $A_2^\pm$  and  $F(\Delta)$  can be found in Appendix C.

The expressions of  $t_p$  and  $|\eta'|$  imply that the transmission spectra can be modified by the power  $P_c$  of control field, magnon-photon coupling strength  $g$ , the coupling parameters  $\eta_a$  and  $\eta_m$ . The adjustment of these parameters will result in different spectra, which arise from the interference between the directly transmitted probe field  $s_p$  and the leakage of the cavity field to the waveguide  $\sqrt{\eta_a \kappa_a} A_-$ . For the first-order Stokes sideband,  $T = |t_p|^2$  can display the amplification, magnomechanically induced absorption and transparency in different parameter regimes. Here we regard the absorption (transparency) as the reduction (enhancement) of the transmission by magnomechanical interaction, while the amplification is referred to the case when the power ratio between the transmission and probe fields is larger than unity [70]. Moreover, an effective window on transmission spectrum induces the group delay. It is caused by the extremely abrupt change of the refractive index and can be calculated as [97]

$$\tau_1 = \frac{d\theta_1}{d\Delta}, \quad \tau_2 = \frac{d\theta_2}{2d\Delta} \quad (71)$$

with  $\theta_1 = \arg[t_p(\Delta)]$  and  $\theta_2 = \arg[\eta'(\Delta)]$  denoting the phases of the output field on the first- and second-order sidebands at the frequency  $\omega_p$ , respectively.

## B. First-order sideband

We now study the tunable output field effects on the first-order sideband. Specifically, we consider the tunable amplification and magnomechanically induced absorption, which can be used to slow and fast light, respectively.

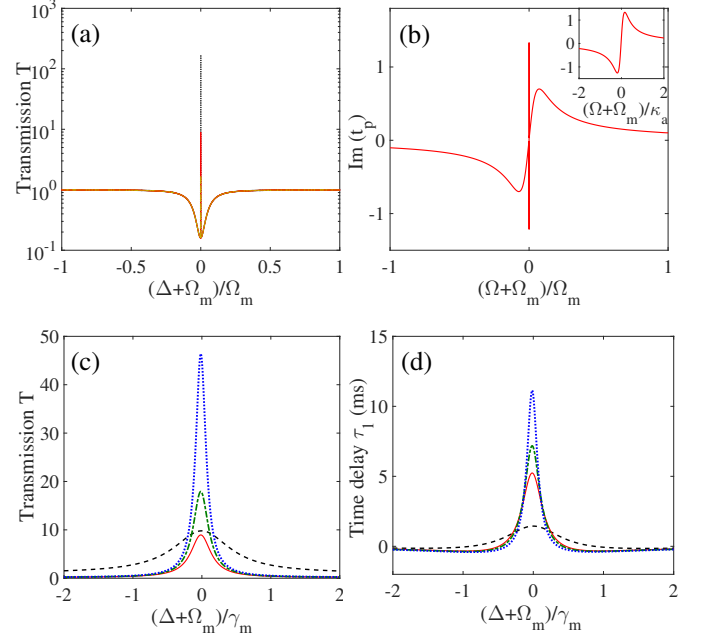


FIG. 5: (Color online) Transmission coefficient  $T$  and dispersion  $\text{Im}(t_p)$  versus the detuning  $\Delta$  for the over-coupling case ( $\eta_a = 0.7$ ) with  $g/\kappa_a = 0.16$  are shown in (a) and (b), respectively. Curves in (a) with different colors represent the transmissions for various magnon-waveguide coupling parameters, e.g.,  $\eta_m = 0.7$  (green-dashed),  $0.5$  (red-solid),  $0.3$  (black dotted), while in (b), (c) and (d), we focus on the case of  $\eta_m = 0.5$ . (c) and (d) show the detailed transmission coefficient  $T$  and time delay  $\tau_1$  around the central peak in (a). We consider four different magnon-photon coupling strengths, e.g.,  $g/\kappa_a = 0$  (black-dashed),  $0.16$  (red-solid),  $0.17$  (green dash-dotted) and  $0.18$  (blue-dotted), respectively. Besides, the power of the control field  $P_c = 7$  dBm and we have moved the origin of coordinate to the Stokes sideband of the control field.

### 1. Amplification and slow light

First, we show the transmission  $T = |t_p|^2$  and dispersion  $\text{Im}(t_p)$  on the first-order sideband with  $g/\kappa_a = 0.16$ , in Figs. 5(a) and 5(b), respectively. Here we consider the over-coupling case, in terms of the cavity-waveguide coupling parameter, e.g.,  $\eta_a = 0.7$ . A remarkable probe amplification and an abrupt variation of the dispersion are found near  $\Delta = -\Omega_m$ .

In Fig. 5(a), we show the transmission  $T$  under different magnon-waveguide coupling parameters  $\eta_m$ . We find that except for different heights of peaks, the transmissions for all cases are amplified on the first-order Stokes sideband, which implies the constructive interference between the directly transmitted probe field and leakage of the cavity field. Thus without loss of generality, we mainly focus on the case of  $\eta_m = 0.5$  in other parts of this subsection. The anomalous dispersive behavior at the very vicinity of  $\Delta = -\Omega_m$  is shown in the inset of Fig. 5(b).

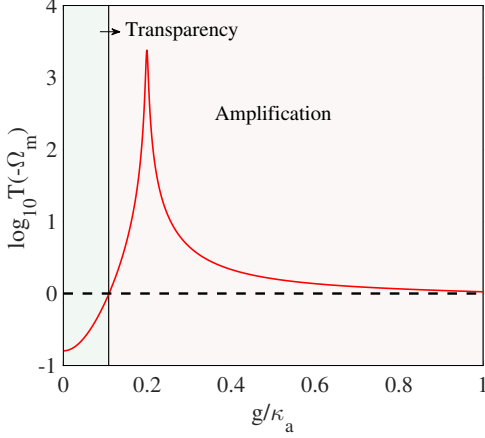


FIG. 6: (Color online) The logarithm of the transmission coefficient on the Stokes sideband  $T(-\Omega_m)$  versus the magnon-photon coupling strength  $g$  for the over-coupling case ( $\eta_a = 0.7$ ). The horizontal black-dashed line represents the transmission  $T(-\Omega_m) = 1$ . Besides, onlind and pink patches are used to label different transmission spectrum regions, i.e., magnomechanical-induced-transparency and nondegenerate parametric amplification, respectively. The other parameters are the same as Fig. 5.

Moreover, the transmissions  $T = |t_p|^2$  versus the detuning  $\Delta = \omega_p - \omega_c$  under different rescaled magnon-photon coupling strengths  $g$  are shown in Fig. 5(c). The sensitivity of the transmission peaks to the magnon-photon coupling strength  $g$  is demonstrated clearly. The black-dashed curve corresponds to the case of  $g = 0$ , i.e., the bare magnomechanical system. As for the cavity magnomechanical system, it can be found that the height of the center peak becomes much higher and narrower with the increase of the magnon-photon coupling strength  $g$ . A growth of 0.02 in the rescaled coupling strength  $g/\kappa_a$ , e.g. from 0.16 (red-solid-dotted line) to 0.18 (blue-dotted line), can induce almost 5.2 times enhancement for the peak of the transmission. As an application, in Fig. 5(d), we show the time delay for different coupling strengths  $g$ . It is obvious that the ability of the system to slow light ( $\tau_1 > 0$ ) can be further enhanced with the increase of  $g$ . When there is no coupling between the cavity and magnon, i.e. for bare magnomechanical system (black-dashed line), the maximum time delay is only 1.4 ms. It can be prolonged for almost eight times to 11 ms, when the magnon-photon coupling reaches  $g/\kappa_a = 0.18$  (blue-dotted line).

Furthermore, in order to show how the transmission of the first-order Stokes sideband  $T(-\Omega_m)$  is affected by the gain of the magnon for the over coupling case, e.g.,  $\eta_a = 0.7$ , we plot the response of the transmission coefficient  $T(-\Omega_m)$  to the magnon-photon coupling strength  $g$  in Fig. 6. We find that the transmission coefficient has been increased for four orders when the rescaled magnon-photon coupling strength approaches to the critical point  $g/\kappa_a \simeq \sqrt{G_m/\kappa_a}/2 = 0.1991$  in the broken

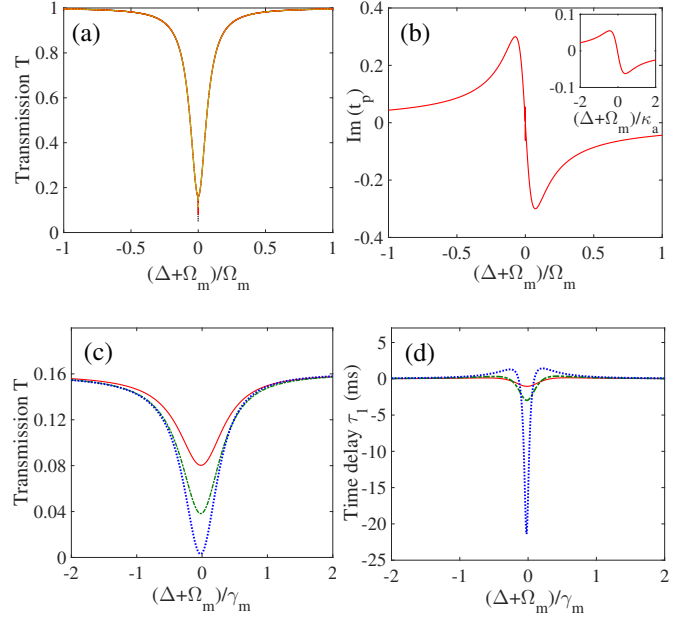


FIG. 7: (Color online) Transmission coefficient  $T$  and dispersion  $\text{Im}(t_p)$  versus the detuning  $\Delta$  for the under-coupling case ( $\eta_a = 0.3$ ) with  $g/\kappa_a = 0.08$  are shown in (a) and (b), respectively. Curves in (a) with different colors represent the transmissions for various magnon-waveguide coupling parameters, e.g.,  $\eta_m=0.7$  (green-dashed), 0.5 (red-solid), 0.3 (black-dotted), while in (b), (c) and (d), we focus on the case of  $\eta_m = 0.5$ . (c) and (d) show the detailed transmission coefficient  $T$  and time delay  $\tau_1$  around the central peak in (a). We consider different magnon-photon coupling strengths, e.g.,  $g/\kappa_a=0.08$  (red-solid), 0.1 (green dash-dotted) and 0.12 (blue-dotted), respectively. Here the power of the control field  $P_c = 7$  dBm and we have moved the origin of coordinate to the Stokes sideband of the control field.

$\mathcal{PT}$ -symmetric phase space, which behaves like the  $\mathcal{PT}$ -symmetric system [35]. Correspondingly, the light can be slowed for about three to four orders compared to the magnomechanical system. Besides, when  $g/\kappa_a$  goes below 0.1081, a transparency window appears in the center of transmission field. This behavior is similar to the electromechanically-induced-transparency shown in conventional optomechanical systems [97–100]. However, in this case, the reduction of the group velocity of light (slow light) is smaller comparing to the nondegenerate parametric amplification regime.

## 2. Magnomechanically induced absorption and fast light

When the cavity-waveguide coupling parameter is tuned to under coupling case, e.g.,  $\eta_a = 0.3$ , we find that the transmission exhibits magnomechanically induced absorption under given magnon-photon coupling strength  $g$ . In this case, the interference between the directly transmitted probe field and leakage of the cav-

ity field is destructive. Similarly, the overall perspectives of the transmissions for different magnon-waveguide coupling parameters  $\eta_m$  are shown in Fig. 7(a). Here the rescaled magnon-photon strength  $g/\kappa_a = 0.08$ . We find that the magnon-waveguide coupling parameter  $\eta_m$  only affects the depths of the dips, but has nothing to do with the lineshape. Thus without loss of generality, we take  $\eta_m = 0.5$  as an example in our analysis below. An apparent dip appears in Fig. 7(a), and its dispersion, which behaves in the normal case at the very vicinity of  $\Delta = -\Omega_m$ , is shown in Fig. 7(b).

In Figs. 7(c) and 7(d), the transmission coefficient  $T$  and time delay  $\tau_1$  around the central dip are plotted as a function of the detuning  $\Delta$  under different magnon-photon coupling strengths  $g$ , respectively. As shown in Fig. 7(c), the dip in the window gets deeper, narrower and almost leads to completely absorption (blue-dotted line) when  $g/\kappa_a$  approaches to 0.12. Meanwhile, the corresponding time delay is decreased from -1 ms (red-solid line) to -21.4 ms (blue-dotted line) in Fig. 7(d) when the rescaled magnon-photon coupling strength  $g/\kappa_a$  is increased from 0.08 to 0.12, denoting stronger ability to fast light ( $\tau_1 < 0$ ).

Moreover, as shown in Fig. 8, the transmission coefficient on the Stokes-sideband  $T(-\Omega_m)$  decreases for about two orders, when the rescaled magnon-photon coupling  $g/\kappa_a$  approaches 0.1254. Similar to the critical point  $g/\kappa_a = 0.1991$  in the amplification region, the critical point  $g/\kappa_a = 0.1254$  in the magnomechanically induced absorption region also locates at the broken  $\mathcal{PT}$  symmetry regime of the  $\mathcal{PT}$ -symmetric-like system. This phenomenon also implies the flexibility to get great suppression of the time delay. Theoretically, the time delay can be decreased almost three orders compared with the magnomechanical system. Note that we do not need strong magnon-photon coupling to get long time delay or accelerate in our system. When  $g/\kappa_a$  locates between 0.1501 and 0.1662, the transmission shows magnomechanically induced transparency, while the amplification occurs when  $g/\kappa_a$  goes over 0.1662.

We have shown that the spectra can go through different regimes by changing the system parameters. The parameter diagrams of these interesting phenomena are plotted in Fig. 9, with the boundary between the transparency and absorption (amplification) regimes labeled by red (blue) curve. When the power  $P_c$  of the control field is settled down to 7 dBm in Fig. 9(a), or for a given magnon-coupling strength, e.g.,  $g/\kappa_a = 0.16$  in Fig. 9(b), the spectra can go through different regimes by tuning the cavity-waveguide coupling parameter  $\eta_a$ . In Figs. 9(c) and 9(d), we give the diagrams for given coupling parameters, e.g.,  $\eta_a = 0.7$  and 0.3, as a function of the magnon-photon coupling strength  $g$  and the power  $P_c$  of the control field, respectively. As shown in Fig. 9(d), it is clear that the magnomechanically induced absorption only occurs for the under coupling case when  $g$  goes to the left of the red curve.

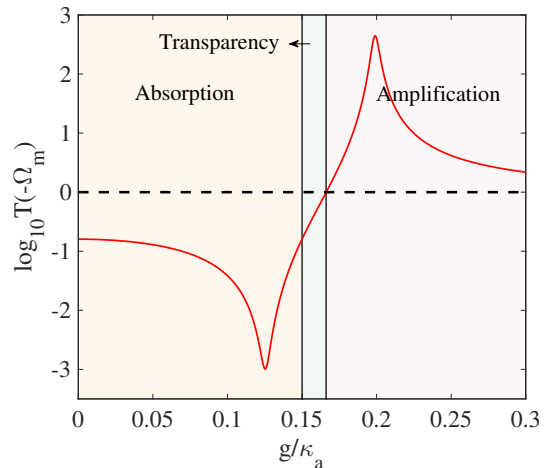


FIG. 8: (Color online) The logarithm of the transmission coefficient on the first-order Stokes sideband  $T(-\Omega_m)$  versus the magnon-photon coupling strength  $g$  for the under-coupling case ( $\eta_a = 0.3$ ). The horizontal black-dashed line represents the transmission  $T(-\Omega_m) = 1$ . Besides, beige, orange and pink patches are used to label different transmission spectra, i.e., magnomechanical induced absorption, transparency and nondegenerate parametric amplification, respectively. The other parameters are the same as Fig. 7.

### C. Second-order sideband

According to Eqs. (70) and (C13-C15), the dimensionless amplitude of the output field for the second-order sideband  $|\eta'|$  is related to the coefficients  $M_1^-$  and  $X_1$  of the first-order Stokes sideband. Thus it is clear that the output field on the second-order sideband will vary following the changes of the first-order sideband.

In Figs. 10(a) and 10(b), we show the variation of the amplitude  $|\eta'|$  and time delay  $\tau_2$  on the second-order sideband with rescaled frequency  $(\Delta + \Omega_m)/\gamma_m$  for the over coupling case ( $\eta_a = 0.7$ ), respectively. Here we consider several different magnon-photon coupling strengths. We find that the peak and linewidth of the spectrum for  $|\eta'|$  becomes higher and narrower with the increase of magnon-photon coupling strength  $g$ . Specifically, the central peak gets more than five times amplification when the rescaled coupling strength  $g/\kappa_a$  is increased from 0.16 (red-solid line) to 0.18 (blue-dotted line). Simultaneously, the time delay  $\tau_2$  is prolonged twice. These trends are similar to the behavior of the transmission  $T$  and time delay  $\tau_1$  on the first-order Stokes sideband, as shown in Figs. 5(c) and 5(d), respectively. This is because that the increase of magnon-photon coupling strength  $g$  causes the amplification of the photon number in the cavity, which further induces the enhancement of the second-order conversion process. Besides, the amplitude  $|\eta'|$  and time delay  $\tau_2$  for the under coupling case ( $\eta_a = 0.3$ ) are shown in Figs. 10(c) and 10(d), respectively. From Figs. 10(a) and 10(c), we find that the amplitudes  $|\eta'|$  for the over

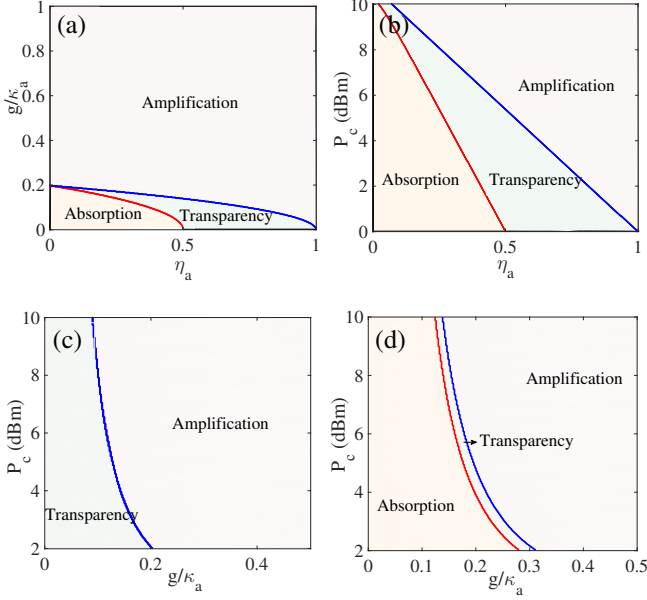


FIG. 9: (Color online) Parametric space diagrams. (a) Parametric space diagram for a given control power  $P_c = 7$  dBm as a function of the coupling parameter  $\eta_a$  and magnon-photon coupling strength  $g$ . (b) Parametric space diagram for a specific magnon-photon coupling strength  $g/\kappa_a = 0.16$  as a function of the coupling parameter  $\eta_a$  and control field power  $P_c$ . Besides, the parametric space diagram as a function of magnon-photon coupling strength  $g$  and control field power  $P_c$  for different coupling parameter, e.g.,  $\eta_a = 0.7$  and  $0.3$  are plotted in (c) and (d), respectively. The red-dashed curve separates the magnomechanical-induced-transparency with the absorption regime, while the blue-dashed curve divides it with the nondegenerate parametric amplification regime.

coupling case  $\eta_a = 0.7$  are almost three times larger than those of the under coupling case  $\eta_a = 0.3$ . We also find that the time delays  $\tau_2$  present almost in the same way for the two cases, as shown in Figs. 10(b) and 10(d). Taking all these facts into account, we use the over coupling case  $\eta_a = 0.7$  as an example in next discussions.

In Fig. 11(a), we show the effect of the cavity-magnon coupling strength  $g$  on the transmission amplitude on the second-order Stokes sideband  $|\eta'(-\Omega_m)|$  from an overall perspective. Significant enhancement of the amplitude  $|\eta'(-\Omega_m)|$  is found when the rescaled cavity-magnon coupling strength  $g/\kappa_a$  is increased to 0.1991, i.e., the critical point in the broken- $\mathcal{PT}$  symmetric regime of the  $\mathcal{PT}$ -symmetric-like system. Actually, the enhancement on the second-order sideband corresponds to the amplification peak on the first-order Stokes sideband shown in Fig. 6. We also give the parameter diagram in Fig. 11(b), which actually corresponds to that of the first-order sideband shown in Fig. 9(c). The interval where the rescaled amplitude  $|\eta'(-\Omega_m)|$  surpasses 1 is highlighted with pink patch and it will get narrower for the under-coupling case.

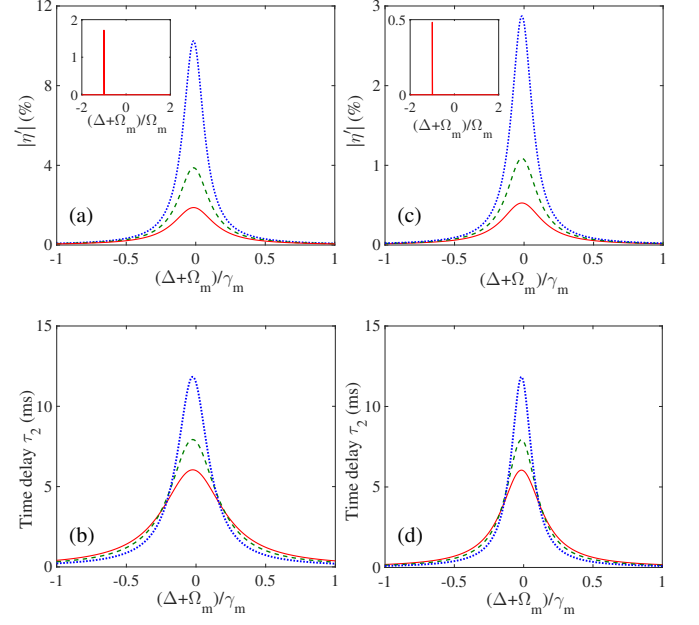


FIG. 10: (Color online) Variations of transmission amplitude  $|\eta'|$  and time delay  $\tau_2$  on the second-order sideband with rescaled frequency  $(\Delta + \Omega_m)/\gamma_m$  in (a) and (b) for the over coupling case ( $\eta_a = 0.7$ ), while in (c) and (d) for the under coupling case ( $\eta_a = 0.3$ ). We consider four different rescaled cavity-magnon coupling strengths, e.g.,  $g/\kappa_a = 0.16$  (red-solid), 0.17 (green-dashed), 0.18 (blue-dotted) and 0.185 (reddish brown dash-dotted), respectively.

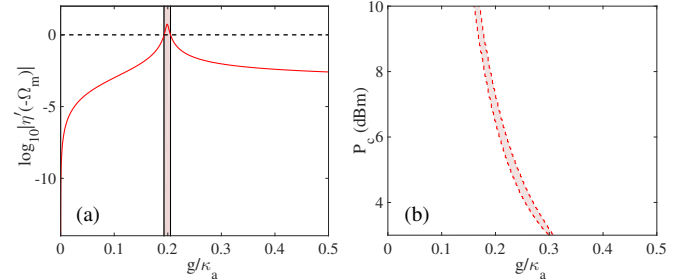


FIG. 11: (Color online) The transmission amplitude on the Stokes sideband  $|\eta'(-\Omega_m)|$  versus the rescaled cavity-magnon coupling strength  $g$  in (a), while the parametric space diagram in (b). Here the cavity-waveguide coupling parameter  $\eta_a = 0.7$ . Pink patches represent the areas where  $|\eta'(-\Omega_m)| > 1$ .

## V. CONCLUSIONS

We have theoretically studied the cavity magnomechanical system, which consists of a yttrium iron garnet (YIG) sphere and a microwave cavity. We show that a  $\mathcal{PT}$ -symmetric-like system can be constructed by the passive cavity mode and active magnon mode, whose effective gain is introduced by resonantly driving the YIG sphere and can be modulated by the power of the driving field, in the cavity magnomechanical system. By chang-

ing the magnon-photon coupling strength, we find that  $\mathcal{PT}$ -symmetric phase transition can occur for the coupled cavity-magnon system in the microwave regime. We mainly study the effect of  $\mathcal{PT}$  symmetry on sideband excitations.

For the transmission of the first-order Stokes sideband, the cavity magnomechanical system has great flexibility to work in different spectrum regimes, as a result of the interference between the directly transmitted probe field and the leakage of the cavity field. The switching between different spectra can be achieved by changing the power of the control field, cavity-waveguide coupling parameter and magnon-photon coupling strength. Compared with the magnomechanical system, we can obtain three to four orders enhancement of the transmission in the amplification (magnomechanically induced absorption) region of the cavity magnomechanical system, when the magnon-photon coupling strength is tuned to the corresponding critical point in the broken  $\mathcal{PT}$  symmetry regime. The ability to slow (fast) light can also be enhanced correspondingly.

Meanwhile, the amplitude and time delay on the second-order sideband also display several orders enhancement at the critical point in the broken  $\mathcal{PT}$  symmetry regime. These phenomena can be attributed to the gain-induced enhancement of the indirect down-conversion from the first-order sideband. These properties provide us alternative perspectives to strengthen the generation of high-order sidebands, which may be inspiring for the study of frequency combs and low-power magnomechanical amplifier.

In summary, we study the interface among microwave, magnonic and mechanical systems, which leads to the low-loss, highly tunable and integrated cavity magnomechanical system. Our research shows that this hybrid system provides a promising platform to the further investigation of  $\mathcal{PT}$ -related-phenomena in microwave system. Our results also lay a theoretical foundation for the enhancement of the magnomechanical-induced high-order sideband frequency comb [101] in the broken  $\mathcal{PT}$  symmetry regime, which is important in the quantum metrology and communications. Our study also indicates the possibility to explore the enhancement of magnon-photon-phonon entanglement [102] in this hybrid cavity magnomechanical system.

### Acknowledgments

Y.X.L and J.Z. are supported by the National Basic Research Program of China (973 Program) under Grant No. 2014CB921401, the Tsinghua University Initiative Scientific Research Program, and the Tsinghua National Laboratory for Information Science and Technology (TNList) Cross-discipline Foundation. J.Z. is supported by the NSFC under Grant Nos. 61622306, 11674194. J.Z. is also supported by the Youth Innovation Fund of Beijing National Research Center for

Information Science and Technology (BNRist). L.Y. is supported by the NSF grant No. EFMA1641109, ARO grant No. W911NF1210026 and ARO grant No. W911NF1710189.

### Appendix A: Hamiltonian of the cavity magnomechanical system

The Hamiltonian schematically shown in Fig. 1 can be written as

$$\mathcal{H}_0 = \mathcal{H}_{free} + \mathcal{H}_{am} + \mathcal{H}_{mp}. \quad (\text{A1})$$

Here  $\mathcal{H}_{free} = \mathcal{H}_a + \mathcal{H}_m + \mathcal{H}_p$  is the free Hamiltonian of the system, with  $\mathcal{H}_a = \omega_a a^\dagger a$ ,  $\mathcal{H}_p = \frac{p^2}{2m_{\text{eff}}} + \frac{1}{2}m_{\text{eff}}\Omega_m^2 x^2$  representing the bare Hamiltonian of cavity and mechanical resonator mode, respectively. They can be obtained by solving the Maxwell equation [103] and elastic equation [104], respectively. As for the YIG sphere, which has a volume of  $V_m$  and magnetization  $\mathbf{M}$ , the static Hamiltonian can be written as

$$\mathcal{H}_m = - \int_{V_m} \mu_0 \mathbf{H} \cdot \mathbf{M} d^3 r. \quad (\text{A2})$$

Here  $\mu_0$  is the magnetic permeability of the free space, and  $\mathbf{H} = H \hat{\mathbf{e}}_z$  is the static magnetic field applied along the  $z$  direction. Besides, the YIG sphere interacts with the cavity magnetic field  $\mathbf{H}'$  in the energy [105]

$$\mathcal{H}_{am} = - \int_{V_m} \mu_0 \mathbf{H}' \cdot \mathbf{M} d^3 r. \quad (\text{A3})$$

On the other hand, the magnetostrictive effect, which describes the deformation of a magnetic material in response to an external magnetic field, can be calculated as [106]

$$\mathcal{H}_{mp} = \frac{b_1}{M_s^2} \int_{V_m} \varepsilon |\mathbf{M}|^2 d^3 r. \quad (\text{A4})$$

Here  $b_1 \approx 3.48 \times 10^6$  erg/cm<sup>3</sup> is the magnetoelastic coupling coefficient and  $M_s$  is the saturation magnetization. The parameter  $\varepsilon$  is the strain tensor of the crystal, with the component

$$\varepsilon_{ij} = \frac{1}{2} \left( \frac{\partial u_i}{\partial x_j} + \frac{\partial u_j}{\partial x_i} \right) \quad (\text{A5})$$

and  $\vec{u}$  representing the displacement.

The YIG sphere with a magnetization  $\mathbf{M}$ , as can be seen experimentally in nanomagnet oscillators of roughly this case [107], acts as a macrospin

$$\mathbf{S} = M V_m / \gamma \equiv (S_+ \hat{\mathbf{e}}_- - S_- \hat{\mathbf{e}}_+) / \sqrt{2} + S_z \hat{\mathbf{e}}_z. \quad (\text{A6})$$

Here we use the helicity basis, i.e.,

$$\hat{\mathbf{e}}_{\pm} = \mp (\hat{x} \pm i \hat{y}) / \sqrt{2}, \quad \hat{\mathbf{e}}_z = \hat{z}. \quad (\text{A7})$$

Furthermore, the macrospin operators are related to the magnon operators via the Holstein-Primakoff transformation [108]

$$S_+ = \left( \sqrt{2S - m^\dagger m} \right) m, \quad (\text{A8})$$

$$S_- = m^\dagger \left( \sqrt{2S - m^\dagger m} \right), \quad (\text{A9})$$

$$S_z = S - m^\dagger m. \quad (\text{A10})$$

Here  $S$  is the total spin number of the macrospin operator and  $m$  ( $m^\dagger$ ) is the annihilation (creation) operator of the magnon mode with resonant frequency  $\omega_m$ . Naturally, for the low-lying excitations with  $\langle m^\dagger m \rangle / 2S \ll 1$ , we have  $S_+ \approx m\sqrt{2S}$ ,  $S_- = m^\dagger\sqrt{2S}$ . Thus with the introduction of magnon mode, the total Hamiltonian of the cavity magnomechanical system now can be written as

$$\begin{aligned} \mathcal{H}_0 = & \hbar\omega_a a^\dagger a + \hbar\omega_m m^\dagger m + \frac{p^2}{2m_{\text{eff}}} + \frac{1}{2}m_{\text{eff}}\Omega_m^2 x^2 \\ & + \hbar g (a^\dagger + a) (m^\dagger + m) + \hbar G x m^\dagger m. \end{aligned}$$

Here, the parameter  $g$  denotes the coupling strength between the cavity and magnon modes, while  $G$  represents the coupling strength between the magnon mode and mechanical resonator. After including the control and probe fields, moving into the rotating reference frame of the control field and conducting the rotating-wave approximation, we finally obtain the Hamiltonian  $\mathcal{H}$  in the main text as shown in Eq. (1).

## Appendix B: Stability of the cavity magnomechanical system

The stability of the magnomechanical system, being similar to the cavity optomechanical system, has been discussed deliberately in [109]. Thus in this section, we mainly focus on steady state of the cavity magnomechanical system. The method can also be reduced to the case of magnomechanical system by making the assumption of  $g = 0$ , i.e., there is no coupling between the magnon and cavity photon.

We have expressed the variables  $a$ ,  $m$ ,  $x$  and  $p$  as the sums of their stable steady-state values and small quantities, which satisfy the mean field and Langevin equations, respectively. First, we only have one real root for the mean field equation shown in Eqs. (61–63) under the resonant driving case, i.e.,  $\bar{\Delta}_m = 0$ . Moreover, the stability of any point in the mean field solutions is established, once the linear Langevin equations, describing the small quantities around this point, are stable. This can be verified by the Routh-Hurwitz criterion [93]. According to the Langevin equations in Eqs. (65–67), we write the dynamical equations of the small quantities up to their first order in the matrix form:

$$\frac{d}{dt} \langle \mathbf{v} \rangle = M \langle \mathbf{v} \rangle + \delta L \quad (\text{B1})$$

where

$$M = \begin{bmatrix} i\Delta_a - \frac{\kappa_a}{2} & 0 & -ig & 0 & 0 & 0 \\ 0 & -i\Delta_a - \frac{\kappa_a}{2} & 0 & ig & 0 & 0 \\ -ig & 0 & i\bar{\Delta}_m - \frac{\kappa_m}{2} & 0 & -iG\bar{m} & 0 \\ 0 & ig & 0 & -i\bar{\Delta}_m - \frac{\kappa_m}{2} & iG\bar{m}^* & 0 \\ 0 & 0 & 0 & 0 & 0 & 1/m_{\text{eff}} \\ 0 & 0 & -\hbar G\bar{m}^* & -\hbar G\bar{m} & -m_{\text{eff}}\Omega_m^2 & -\gamma_m \end{bmatrix} \quad (\text{B2})$$

with

$$\mathbf{v} = [\delta a, \delta a^\dagger, \delta m, \delta m^\dagger, \delta x, \delta p], \quad (\text{B3})$$

$$\delta L = [\sqrt{\eta_a \kappa_a} s_p e^{-i\Delta t}, 0, 0, 0, 0, 0]. \quad (\text{B4})$$

The stability of the system is ensured if all the eigenvalues of matrix  $M$  have negative real parts. Among the three pairs of conjugate eigenvalues, we numerically find that two of them always have negative parts for the total regime we consider. Thus we mainly focus on the remaining one. In Fig. B1, the real parts of its eigenvalue  $\text{Re}(\lambda)$  with different control field powers are plotted as a function of magnon-photon coupling strength  $g$ . The maximum rescaled coupling strength  $g/\kappa_a$  allowed for negative  $\text{Re}(\lambda)$  is 0.2352 for  $P_c = 5$  dBm, while 0.1991 for  $P_c = 7$  dBm. Obviously, the system has larger

stable region for lower control field power. In fact, the threshold for the stable region corresponds to the maximum amplification for the transmission field, where we can also get largest time delay. As shown in Fig. B2, the zero point of the blue-solid line and the maximum of the red-solid line occur at the same critical coupling strength  $g/\kappa_a = 0.1991$ . Besides, the coupling parameter  $\eta_a$  has nothing to do with the matrix  $M$ . This phenomenon implies that the magnon-induced-absorption and transparency always work in the stable regime. Thus we can safely conclude that our proposal allows sufficient large transmission amplification (absorption) and light slow (fast) within the stable regime. Specifically, usually three to four orders larger than case of the bare magnomechanical system, whose transmission coefficient  $T = 10$  and

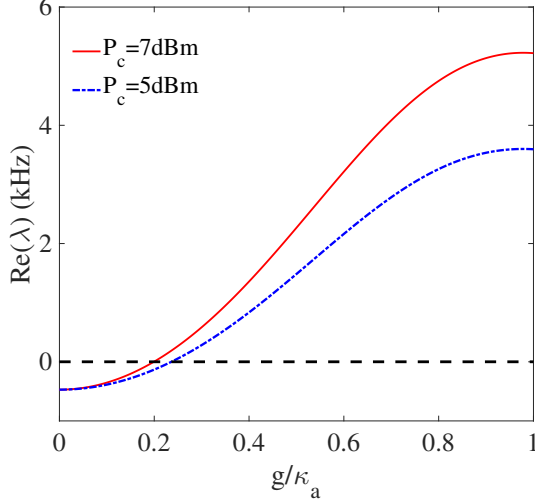


FIG. B1: (Color online) The real part of the eigenvalues  $\text{Re}(\lambda)$  of the matrix  $M$  in Eq. (B2) versus the magnon-photon coupling strength with different control power  $P_c = 5$  dBm (blue-dash-dotted line) and 7 dBm (red-solid line). The horizontal black-dashed line represents  $\text{Re}(\lambda) = 0$ , and it separates the stable (below) and unstable (above) region.

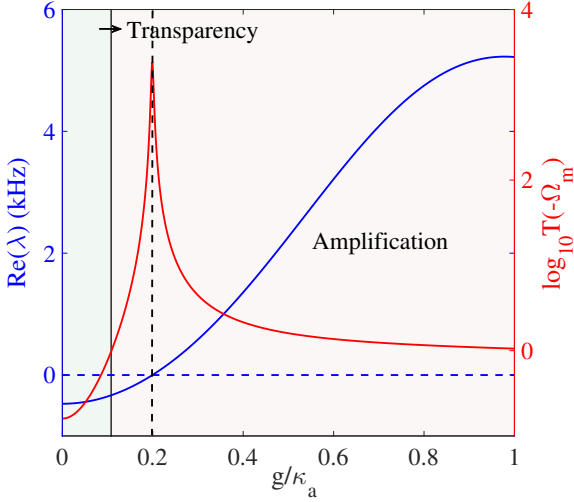


FIG. B2: (Color online) The real part of the eigenvalues  $\text{Re}(\lambda)$  of the matrix  $M$  in Eq. (B2) (blue-solid line) and the logarithm of the transmission coefficient on the Stokes sideband  $T(-\omega_m)$  versus the magnon-photon coupling strength  $g$  under the control power  $P_c = 7$  dBm. Ondine and pink patches are used to label different transmission spectra regions, i.e., magnomechanical-induced-transparency and non-degenerate parametric amplification, respectively. The horizontal blue-dashed line corresponds to  $\text{Re}(\lambda) = 0$ , while the vertical black-dashed line represents the peak of the transmission  $\log_{10} T(-\Omega_m)$ .

time delay  $\tau_1 = 1$  ms on the first-order Stokes sideband.

### Appendix C: Amplitudes of the transmitted field for the total cavity magnomechanical system

To obtain solutions of Eqs. (65-67), we make the following ansatz

$$\langle \delta a \rangle = A_1^- e^{-i\Delta t} + A_1^+ e^{i\Delta t} + A_2^- e^{-2i\Delta t} + A_2^+ e^{2i\Delta t} \quad (C1)$$

$$\langle \delta a^\dagger \rangle = (A_1^+)^* e^{-i\Delta t} + (A_1^-)^* e^{i\Delta t} + (A_2^+)^* e^{-2i\Delta t} + (A_2^-)^* e^{2i\Delta t}, \quad (C2)$$

$$\langle \delta m \rangle = M_1^- e^{-i\Delta t} + M_1^+ e^{i\Delta t} + M_2^- e^{-2i\Delta t} + M_2^+ e^{2i\Delta t}, \quad (C3)$$

$$\langle \delta m^\dagger \rangle = (M_1^+)^* e^{-i\Delta t} + (M_1^-)^* e^{i\Delta t} + (M_2^+)^* e^{-2i\Delta t} + (M_2^-)^* e^{2i\Delta t}, \quad (C4)$$

$$\langle \delta x \rangle = X_1 e^{-i\Delta t} + X_1^* e^{i\Delta t} + X_2 e^{-2i\Delta t} + X_2^* e^{2i\Delta t} \quad (C5)$$

to the second order sideband. By substituting the ansatz into Eqs. (65-67) and grouping the terms of the same frequency, we can obtain the solutions of the amplitudes for the first-order sideband as

$$A_1^- = F(\Delta) \sqrt{\eta_a \kappa_a} s_p, \quad (C6)$$

$$M_1^- = i [\lambda_a(\Delta) A_1^- - \sqrt{\eta_a \kappa_a} s_p] g^{-1}, \quad (C7)$$

$$X_1^- = -(gG\bar{m})^{-1} \lambda_a(\Delta) \Lambda(\Delta) A_1^- + (gG\bar{m})^{-1} \lambda_m(\Delta) \sqrt{\eta_a \kappa_a} s_p, \quad (C8)$$

with

$$F(\Delta) = \frac{-1 + R(\Delta) \lambda_m(\Delta)}{\lambda_a(\Delta) [-1 + R(\Delta) \Lambda(\Delta)]}, \quad (C9)$$

and

$$\Lambda(\Delta) = [\lambda_m(\Delta) \lambda_a(\Delta) + g^2] [\lambda_a(\Delta)]^{-1}, \quad (C10)$$

$$R(\Delta) = [\Lambda^\dagger(\Delta)]^{-1} - i[\hbar\chi(\Delta) G^2 \bar{m}^2]^{-1}. \quad (C11)$$

The function

$$\lambda_a(\Delta) = -i(\Delta_a + \Delta) + \frac{\kappa_a}{2} \quad (C12)$$

in Eq. (C9) denotes the cavity response. Similarly, the amplitudes of the second-order sideband, which are composed of the direct down-conversion of control field and indirect down-conversion of first-order sideband, can be obtained as

$$M_2^- = N_n(\Delta) [N_d(\Delta)]^{-1} \quad (C13)$$

$$A_2^- = -ig [\lambda_a(2\Delta)]^{-1} M_2^-, \quad (C14)$$

with

$$N_n(\Delta) = -G \left\{ i [\Lambda^\dagger(2\Delta) - \Lambda^\dagger(\Delta)] F^{(2)}(\Delta) + 1 \right\} M_1^- X_1 + G^2 \bar{m}^* F^{(2)}(\Delta) X_1^2, \quad (C15)$$

$$N_d(\Delta) = F^{(2)}(\Delta) \Lambda^\dagger(\Delta) [\Lambda^\dagger(2\Delta) - \Lambda(2\Delta)] - i\Lambda(2\Delta), \quad (C16)$$

and

$$F^{(2)}(\Delta) = -\frac{\hbar G^2 |\bar{m}|^2 \chi(2\Delta)}{\Lambda^\dagger(\Delta) \Lambda^\dagger(2\Delta)}. \quad (\text{C17})$$

Here,  $\lambda(\Delta)$  and  $\chi(\Delta)$  can be obtained from Eqs. (31) and (30) with the replacement of  $\Delta'$  by  $\Delta$ , correspond-

ingly. The function  $\Lambda^\dagger(\Delta)$  is the complex conjugate of  $\Lambda(\Delta)$ .

- 
- [1] C. M. Bender and S. Boettcher, Real spectra in non-Hermitian Hamiltonians having  $\mathcal{PT}$  symmetry, *Phys. Rev. Lett.* **80**, 5243-5246 (1998).
- [2] C. M. Bender, D. C. Brody, and H. F. Jones, Complex extension of quantum mechanics, *Phys. Rev. Lett.* **89**, 270401 (2002).
- [3] N. Hatano and D. R. Nelson, Localization transitions in non-hermitian quantum mechanics, *Phys. Rev. Lett.* **77**, 570-573 (1996).
- [4] R. El-Ganainy, K. G. Makris, D. N. Christodoulides, and Z. H. Musslimani, Theory of coupled optical  $\mathcal{PT}$ -symmetric structures, *Opt. Lett.* **32**, 26322634 (2007).
- [5] K. G. Makris, R. El-Ganainy, D. N. Christodoulides, and Z. H. Musslimani, Beam dynamics in  $\mathcal{PT}$  symmetric optical lattices, *Phys. Rev. Lett.* **100**, 103904 (2008).
- [6] C. E. Rüter, K. G. Makris, R. El-Ganainy, D. N. Christodoulides, M. Segev and D. Kip, Observation of parity-time symmetry in optics, *Nat. Phys.* **6**, 192195 (2010)
- [7] O. Bendix, R. Fleischmann, T. Kottos, and B. Shapiro, Exponentially fragile  $\mathcal{PT}$  symmetry in lattices with localized eigenmodes, *Phys. Rev. Lett.* **103**, 030402 (2009).
- [8] S. Longhi, Bloch oscillations in complex crystals with  $\mathcal{PT}$  symmetry, *Phys. Rev. Lett.* **103**, 123601 (2009).
- [9] C. T. West, T. Kottos, and T. Prosen,  $\mathcal{PT}$ -symmetric wave chaos, *Phys. Rev. Lett.* **104**, 054102 (2010).
- [10] E.-M. Graefe, and H. F. Jones,  $\mathcal{PT}$ -symmetric sinusoidal optical lattices at the symmetry-breaking threshold, *Phys. Rev. A* **84**, 013818 (2011).
- [11] C. M. Bender,  $\mathcal{PT}$  symmetry in quantum physics: from a mathematical curiosity to optical experiments, *Europhys. News* **47**, 17-20 (2016).
- [12] A. Guo, G. J. Salamo, D. Duchesne, R. Morandotti, M. Volatier-Ravat, V. Aimez, G. A. Siviloglou, and D. N. Christodoulides, Observation of  $\mathcal{PT}$ -symmetry breaking in complex optical potentials, *Phys. Rev. Lett.* **103**, 093902 (2009).
- [13] M. Lawrence, N. Xu, X. Zhang, L. Cong, J. Han, W. Zhang, and S. Zhang, Manifestation of  $\mathcal{PT}$  symmetry breaking in polarization space with terahertz metasurfaces, *Phys. Rev. Lett.* **113**, 093901 (2014).
- [14] Y. Xu, W. S. Fegadolli, L. Gan, M. Lu, X. Liu, Z. Li, A. Scherer, and Y. Chen, Experimental realization of Bloch oscillations in a parity-time synthetic silicon photonic lattice, *Nat. Commun.* **7**, 11319 (2016).
- [15] H. Zhao, W. S. Fegadolli, J. Yu, Z. Zhang, L. Ge, A. Scherer, and L. Feng, Metawaveguide for asymmetric interferometric light-light switching, *Phys. Rev. Lett.* **117**, 193901 (2016).
- [16] L. Feng, Z. J. Wong, R.-M. Ma, Y. Wang, and X. Zhang, Single-mode laser by parity-time symmetry breaking, *Science* **346**, 972975 (2014).
- [17] B. Peng, Ş. K. Özdemir, F. C. Lei, F. Monifi, M. Gianfreda, G. L. Long, S. H. Fan, F. Nori, C. M. Bender, and L. Yang, Parity-time-symmetric whispering-gallery microcavities, *Nat. Phys.* **10**, 394398 (2014).
- [18] M. Brandstetter, M. Liertzer, C. Deutsch, P. Klang, J. SchÖberl, H. E. Türeci, G. Strasser, K. Unterrainer and S. Rotter, Reversing the pump dependence of a laser at an exceptional point, *Nat. Commun.* **5**, 4034 (2014).
- [19] J. Doppler, A. A. Mailybaev, J. Böhm, U. Kuhl, A. Girschik, F. Libisch, T. J. Milburn, P. Rabl, N. Moiseyev, and S. Rotter, Dynamically encircling an exceptional point for asymmetric mode switching, *Nature* **537**, 76-79 (2016).
- [20] J. Schindler, A. Li, Mei C. Zheng, F. M. Ellis, and T. Kottos, Experimental study of active LRC circuits with  $\mathcal{PT}$  symmetries, *Phys. Rev. A* **84**, 040101(R) (2011).
- [21] J. Schindler, Z. Lin, J. M. Lee, H. Ramezani, F. M. Ellis and T. Kottos,  $\mathcal{PT}$ -symmetric electronics, *J. Phys. A* **45**, 444029 (2012).
- [22] H. Ramezani, D. N. Christodoulides, V. Kovanis, I. Vitebskiy, and T. Kottos,  $\mathcal{PT}$ -symmetric Talbot effect. *Phys. Rev. Lett.* **109**, 033902 (2012).
- [23] H. Ramezani, J. Schindler, F. M. Ellis, U. Gunther, and T. Kottos, Bypassing the bandwidth theorem with  $\mathcal{PT}$ -symmetry, *Phys. Rev. A* **85**, 062122 (2012).
- [24] R. Fleury, D. Sounas, and A. Alú, An invisible acoustic sensor based on parity-time symmetry, *Nat. Commun.* **6**, 5905 (2014).
- [25] X. Zhu, H. Ramezani, C. Shi, J. Zhu, and X. Zhang,  $\mathcal{PT}$ -symmetric acoustics, *Phys. Rev. X* **4**, 031042 (2014).
- [26] C. Z. Shi, M. Dubois, Y. Chen, L. Cheng, H. Ramezani, Y. Wang, and X. Zhang, Accessing the exceptional points of parity-time symmetric acoustics, *Nat. Commun.* **7**, 11110 (2016).
- [27] J. Zhang, B. Peng, Ş. K. Özdemir, Y.-X. Liu, H. Jing, X.-Y. Lü, Y.-L. Liu, L. Yang, and F. Nori, Giant non-linearity via breaking parity-time symmetry: A route to low-threshold phonon diodes, *Phys. Rev. B* **92**, 115407 (2015).
- [28] H. Xu, D. Mason, L. Jiang, and J. G. E. Harris, Topological energy transfer in an optomechanical system with exceptional points, *Nature* **537**(7618), 8083 (2016).
- [29] H. Jing, Ş. K. Özdemir, X.-Y. Lü, J. Zhang, L. Yang, and F. Nori,  $\mathcal{PT}$ -symmetric phonon laser, *Phys. Rev. Lett.* **113**, 053604 (2014)
- [30] J. Zhang, B. Peng, Ş. K. Özdemir, K. Pichler, D. O. Krimer, G. Zhao, F. Nori, Y. Liu, S. Rotter and L. Yang, A Phonon laser operating at an exceptional point, *Nature Photon.* **12**, 479-484 (2018).

- [31] H. Lü, Ş. K. Özdemir, L. M. Kuang, F. Nori, and H. Jing, Exceptional points in random-defect phonon lasers, *Phys. Rev. Appl.* **8**(4), 044020 (2017).
- [32] H. Jing, Ş. K. Özdemir, Z. Geng, J. Zhang, X.-Y. Lü, B. Peng, L. Yang, and F. Nori, Optomechanically-induced transparency in parity-time-symmetric microresonators, *Sci. Rep.* **5**, 9663 (2015).
- [33] W. Li, Y. Jiang, C. Li, and H. Song, Parity-time-symmetry enhanced optomechanically induced transparency, *Sci. Rep.* **6**, 31095(2016)
- [34] X. Y. Zhang, Y. Q. Guo, P. Pei, and X. X. Yi, Optomechanically induced absorption in parity-time-symmetric optomechanical systems, *Phys. Rev. A* **95**, 063825 (2017).
- [35] Y.-L. Liu, R. Wu, J. Zhang, Ş. K. Özdemir, L. Yang, F. Nori, and Y. X. Liu, Controllable optical response by modifying the gain and loss of a mechanical resonator and cavity mode in an optomechanical system, *Phys. Rev. A* **95**, 013843 (2017).
- [36] L. Chang, X. Jiang, S. Hua, C. Yang, J. Wen, L. Jiang, G. Li, G. Wang, and M. Xiao, Parity-time symmetry and variable optical isolation in active-passive-coupled microresonators, *Nat. Photon.* **8**, 524529 (2014).
- [37] Z. Lin, H. Ramezani, T. Eichelkraut, T. Kottos, H. Cao, and D. N. Christodoulides, Unidirectional invisibility induced by  $\mathcal{PT}$ -symmetric periodic structures, *Phys. Rev. Lett.* **106**, 213901 (2011).
- [38] A. Regensburger, C. Bersch, M. Miri, G. Onishchukov, D. N. Christodoulides, and U. Peschel, Parity-time synthetic photonic lattices, *Nature*. **488**, 167 (2012).
- [39] L. Feng, Y. L. Xu, W. S. Fegadolli, M. H. Lu, J. E. B. Oliveira, V. R. Almeida, Y.-F. Chen, and A. Scherer, Experimental demonstration of a unidirectional reflectionless parity-time metamaterial at optical frequencies, *Nat. Mater.* **12**, 108 (2013).
- [40] J. Li, X. Zhan, C. Ding, D. Zhang, and Y. Wu, Enhanced nonlinear optics in coupled optical microcavities with an unbroken and broken parity-time symmetry, *Phys. Rev. A* **92**, 043830 (2015).
- [41] S. K. Gupta and A. K. Sarma, Peregrine rogue wave dynamics in the continuous nonlinear Schrödinger system with parity-time symmetric Kerr nonlinearity, *Commun. Nonlinear Sci. Numer. Simul.* **36**, 141 (2016).
- [42] X. Y. Lü, H. Jing, J. Y. Ma, and Y. Wu,  $\mathcal{PT}$ -symmetry-breaking chaos in optomechanics, *Phys. Rev. Lett.* **114**, 253601 (2015).
- [43] Y. D. Chong, Li Ge, and A. D. Stone,  $\mathcal{PT}$ -symmetry breaking and laser-absorber modes in optical scattering systems, *Phys. Rev. Lett.* **108**, 269902 (2012).
- [44] Y. Sun, W. Tan, H. Li, J. Li, and H. Chen, Experimental Demonstration of a coherent perfect absorber with  $\mathcal{PT}$  phase transition, *Phys. Rev. Lett.* **112**, 143903 (2014).
- [45] Z.-P. Liu, J. Zhang, Ş. K. Özdemir, B. Peng, H. Jing, X.-Y. Lü, C.-W. Li, L. Yang, F. Nori, and Y.-X. Liu, Metrology with  $\mathcal{PT}$ -symmetric cavities: enhanced sensitivity near the  $\mathcal{PT}$ -phase transition, *Phys. Rev. Lett.* **117**, 110802 (2016).
- [46] W. Chen, J. Zhang, B. Peng, Ş. K. Özdemir, X.-D. Fan, and L. Yang, Parity-time-symmetric whispering-gallery mode nanoparticle sensor, *Photon. Res.* **6**(5), A23-A30 (2018).
- [47] W. Chen, Ş. K. Özdemir, G. Zhao, J. Wiersig and L. Yang, Exceptional points enhance sensing in an optical microcavity, *Nature* **548**, 192-196 (2017).
- [48] S. V. Dmitriev, A. A. Sukhorukov, and Yu. S. Kivshar, Binary parity-time-symmetric nonlinear lattices with balanced gain and loss, *Opt. Lett.* **35**, 2976 (2010).
- [49] H. Ramezani, D. N. Christodoulides, V. Kovanis, I. Vitebskiy, and T. Kottos,  $\mathcal{PT}$ -Symmetric Talbot Effects, *Phys. Rev. Lett.* **109**, 033902 (2012).
- [50] N. Lazarides and G. P. Tsironis, Gain-driven discrete breathers in  $\mathcal{PT}$ -symmetric nonlinear metamaterials, *Phys. Rev. Lett.* **110**, 053901 (2013).
- [51] S. Bittner, B. Dietz, U. Günther, H. L. Harney, M. Miski-Oglu, A. Richter, and F. Schäfer,  $\mathcal{PT}$  Symmetry and Spontaneous Symmetry Breaking in a Microwave Billiard, *Phys. Rev. Lett.* **108**, 024101 (2012).
- [52] F. Quijandria, U. Naether, Ş. K. Özdemir, F. Nori, and D. Zueco,  $\mathcal{PT}$ -symmetric circuit QED, *Phys. Rev. A*. **97**, 053846 (2018).
- [53] Ö. O. Soykal and M. E. Flatté, Strong Field Interactions between a Nanomagnet and a Photonic cavity, *Phys. Rev. Lett.* **104**, 077202 (2010).
- [54] Ö. O. Soykal and M. E. Flatté, Size dependence of strong coupling between nanomagnets and photonic cavities, *Phys. Rev. B*. **82**, 104413 (2010).
- [55] B. M. Yao, Y. S. Gui, Y. Xiao, H. Guo, X. S. Chen, W. Lu, C. L. Chien, and C.-M. Hu, Theory and experiment on cavity magnon-polariton in the one-dimensional configuration, *Phys. Rev. B* **92**, 184407 (2015).
- [56] L. V. Abdurakhimov, Y. M. Bunkov, and D. Konstantinov, Normal-mode splitting in the coupled system of hybridized nuclear magnons and microwave photons, *Phys. Rev. Lett.* **114**, 226402 (2015).
- [57] B. Z. Rameshti, Y. Cao, and G. E. W. Bauer, Magnetic spheres in microwave cavities, *Phys. Rev. B* **91**, 214430 (2015).
- [58] B. Wang, Z.-X. Liu, C. Kong, H. Xiong and Y. Wu, Magnon-induced transparency and amplification in  $\mathcal{PT}$ -symmetric cavity-magnon system, *Opt. Express* **26**, 20248 (2018).
- [59] D. Zhang, X.-Q. Luo, Y.-P. Wang, T.-F. Li, and J.-Q. You, Observation of the exceptional point in cavity magnon-polaritons, *Nat. Commun.* **8**, 1368 (2017).
- [60] J.-G. Zhu, G.-M. Zhao, I. Savukov, and L. Yang, Polymer encapsulated microcavity optomechanical magnetometer, *Sci. Rep.* **7**, 8896 (2017).
- [61] H. Huebl, C. W. Zollitsch, J. Lotze, F. Hocke, M. Greifenstein, A. Marx, R. Gross, and S. T. B. Goennenwein, High Cooperativity in Coupled Microwave Resonator Ferrimagnetic Insulator Hybrids, *Phys. Rev. Lett.* **111**, 127003 (2013).
- [62] Y. Tabuchi, S. Ishino, T. Ishikawa, R. Yamazaki, K. Usami, and Y. Nakamura, Hybridizing Ferromagnetic Magnons and Microwave Photons in the Quantum Limit, *Phys. Rev. Lett.* **113**, 083603 (2014).
- [63] X. Zhang, C.-L. Zou, L. Jiang, and H. X. Tang, Strongly Coupled Magnons and Cavity Microwave Photons, *Phys. Rev. Lett.* **113**, 156401 (2014).
- [64] M. Goryachev, W. G. Farr, D. L. Creedon, Y. Fan, M. Kostylev, and M. E. Tobar, High-Cooperativity Cavity QED with Magnons at Microwave Frequencies, *Phys. Rev. Appl.* **2**, 054002 (2014).
- [65] L. Bai, M. Harder, Y. P. Chen, X. Fan, J. Q. Xiao, and C.-M. Hu, Spin Pumping in Electrodynamically Coupled Magnon-Photon Systems, *Phys. Rev. Lett.* **113**,

- 227201 (2015).
- [66] D. Zhang, X.-M. Wang, T.-F. Li, X.-Q. Luo, W. Wu, F. Nori, and J.-Q. You, Cavity quantum electrodynamics with ferromagnetic magnons in a small yttrium-iron-garnet sphere, *NPJ Quantum Inf.* **1**, 15014 (2015).
- [67] X. Zhang, C.-L. Zou, N. Zhu, F. Marquardt, L. Jiang and H. X. Tang, Magnon dark modes and gradient memory, *Nat. Commun.* **6**, 8914 (2015).
- [68] Y. Tabuchi, S. Ishino, A. Noguchi, T. Ishikawa, R. Yamazaki, K. Usami, Y. Nakamura, Coherent coupling between a ferromagnetic magnon and a superconducting qubit, *Science* **349**, 405 (2015).
- [69] Y. Tabuchi, S. Ishino, A. Noguchi, T. Ishikawa, R. Yamazaki, K. Usami, Y. Nakamura, Quantum magnonics: The magnon meets the superconducting qubit, *C. R. Phys.* **17** (2016).
- [70] X. Zhang, C.-L. Zou, L. Jiang, and H. X. Tang, Cavity magnomechanics, *Sci. Adv.* **2**, 1501286 (2016).
- [71] Y. Yu, S. Forstner, H. Rubinsztein-Dunlop, W. P. Bowen, Modelling of Cavity Optomechanical Magnetometers, *Sensors* **18**, 1558 (2018).
- [72] V. B. Braginsky, S. E. Strigin, and S. P. Vyatchanin, Parametric oscillatory instability in Fabry-Perot interferometer, *Phys. Lett. A* **287**, 331 (2001).
- [73] M. Poot, K. Y. Fong, M. Bagheri, W. H. P. Pernice, and H. X. Tang, Backaction limits on self-sustained optomechanical oscillations, *Phys. Rev. A* **86**, 053826 (2012).
- [74] F. Marquardt, J. G. E. Harris, and S. M. Girvin, Dynamical multistability induced by radiation pressure in high-finesse micromechanical optical cavities, *Phys. Rev. Lett.* **96**, 103901(2006).
- [75] J. Qian, A. A. Clerk, K. Hammerer, and F. Marquardt, Quantum Signatures of the Optomechanical Instability, *Phys. Rev. Lett.* **109**, 253601 (2012).
- [76] H. Z. Wu, G. Heinrich, and F. Marquardt, The effect of Landau-Zener dynamics on phonon lasing, *New J. Phys.* **15**, 123022 (2013).
- [77] T. J. Kippenberg, H. Rokhsari, T. Carmon, A. Scherer, and K. J. Vahala, Analysis of radiation-pressure induced mechanical oscillation of an optical microcavity, *Phys. Rev. Lett.* **95**, 033901 (2005).
- [78] G. Anetsberger, O. Arcizet, Q. P. Unterreithmeier, R. Rivière, A. Schliesser, E. M. Weig, J. P. Kotthaus, and T. J. Kippenberg, Near-field cavity optomechanics with nanomechanical oscillators, *Nat. Phys.* **5**, 909 (2009).
- [79] I. S. Grudin, H. Lee, O. Painter, and K. J. Vahala, Phonon Laser Action in a Tunable Two-Level System, *Phys. Rev. Lett.* **104**, 083901 (2010).
- [80] X. W. Xu, Y. X. Liu, C. P. Sun, and Y. Li, Mechanical  $\mathcal{PT}$  symmetry in coupled optomechanical systems, *Phys. Rev. A* **92**, 013852 (2015).
- [81] W. L. Li, C. Li, and H. S. Song, Theoretical realization and application of parity-time-symmetric oscillators in a quantum regime, *Phys. Rev. A* **95**, 023827 (2017).
- [82] Y. Jiao, H. Lü, J. Qian, and H. Jing, Nonlinear optomechanics with gain and loss: amplifying higher-order sideband and group delay, *New J. Phys.* **18**, 083034 (2016).
- [83] S. Weis, R. Rivière, S. Deléglise, E. Gavartin, O. Arcizet, A. Schliesser, and T. J. Kippenberg, Optomechanically induced transparency, *Science* **330**, 1520 (2010).
- [84] M. O. Scully and M. S. Zubairy, *Quantum Optics* (Cambridge University Press, Cambridge, 1997)..
- [85] Y.-P. Wang, G.-Q. Zhang, D. Zhang, X.-Q. Luo, W. Xiong, S.-P. Wang, T.-F. Li, C.-M. Hu, and J. Q. You, Magnon Kerr effect in a strongly coupled cavity-magnon system, *Phys. Rev. B* **94**, 224410 (2016).
- [86] C. W. Gardiner, *Quantum Noise* (Springer-Verlag, Berlin, 1991), Chap. 3.
- [87] V. Giovannetti and D. Vitali, Phase-noise measurement in a cavity with a movable mirror undergoing quantum Brownian motion, *Phys. Rev. A* **63**, 023812 (2001).
- [88] H. Xiong, L.-G. Si, A.-S. Zheng, X. Yang and Y. Wu, Higher-order sidebands in optomechanically induced transparency, *Phys. Rev. A* **86**, 013815 (2012).
- [89] J. H. Li, J. H. Li, Q. Xiao, and Y. Wu, Giant enhancement of optical high-order sideband generation and their control in a dimer of two cavities with gain and loss, *Phys. Rev. A* **93**, 063814 (2016).
- [90] Y.-F. Jiao, T.-X. Lu, and H. Jing, Optomechanical second-order sidebands and group delays in a Kerr resonator, *Phys. Rev. A* **97**, 013843 (2018).
- [91] R. W. Boyd, *Nonlinear Optics*, 3rd ed. (Elsevier, 2008)
- [92] C. W. Gardiner and M. J. Collett, Input and output in damped quantum systems: Quantum stochastic differential equations and the master equation, *Phys. Rev. A* **31**, 3761 (1985).
- [93] E. X. DeJesus and C. Kaufman, Routh-Hurwitz criterion in the examination of eigenvalues of a system of nonlinear ordinary differential equations, *Phys. Rev. A* **35**, 5288-5920 (1987).
- [94] J. Stein, in *Digital Signal Processing: A computer Science Perspective*, edited by J. G. Proakis (Wiley, 2000), p. 115.
- [95] H. Lü, C.-Q. Wang, L. Yang, and H. Jing, Optomechanically Induced Transparency at Exceptional Points, *Phys. Rev. Appl.* **10**, 014006 (2018).
- [96] H. Zhang, F. Saif, Y. Jiao, and H. Jing, Loss-induced transparency in optomechanics, arXiv:1807.10538v1.
- [97] A. H. Safavi-Naeini, T. P. M. Alegre, J. Chan, M. Eichenfield, M. Winger, Q. Lin, J. T. Hill, D. E. Chang, and O. Painter, Electromagnetically induced transparency and slow light with optomechanics, *Nature (London)* **472**, 69 (2011).
- [98] M. Karuza, C. Biancofiore, M. Bawaj, C. Molinelli, M. Galassi, R. Natali, P. Tombesi, G. Di Giuseppe, and D. Vitali, Optomechanically induced transparency in a membrane-in-the-middle setup at room temperature, *Phys. Rev. A* **88**, 013804 (2013).
- [99] F. Massel, S. U. Cho, J. M. Pirkkalainen, P. J. Hakonen, T. T. Heikkilä, and M. A. Sillanpää, Multimode circuit optomechanics near the quantum limit, *Nat. Commun.* **3**, 987 (2012).
- [100] X. Zhou, F. Hocke, A. Schliesser, A. Marx, H. Huebl, R. Gross, and T. J. Kippenberg, Slowing, advancing and switching of microwave signals using circuit nanoelectromechanics, *Nat. Phys.* **9**, 179 (2013).
- [101] Z.-X. Liu, B. Wang, H. Xiong, and Y. Wu, Magnon-induced high-order sideband generation, arXiv:1806.08289v2.
- [102] J. Li, S.-Y. Zhu, and G. S. Agarwal, Magnon-phonon-phonon entanglement in cavity magnomechanics, arXiv:1807.07158v1.
- [103] W. Heitler, *The Quantum theory of Radiation*, 3rd ed. (Dover, New York, 1998).
- [104] A. N. Cleland, *The Foundations of Nanomechanics: From Solid-State Theory to Device Applications* (Springer-Verlag, New York, 2003).
- [105] J. D. Jackson, *Classical Electrodynamics*, 3rd ed. (Wi-

- ley, New York, 1998).
- [106] H. Keshtgar, M. Zareyan, G. E. W. Bauer, Acoustic parametric pumping of spin waves, *Solid State Commun.* **198**, 3034 (2014).
- [107] J. C. Sankey, P. M. Braganca, A. G. F. Garcia, I. N. Krivorotov, R. A. Buhrman, and D. C. Ralph, Spin-Transfer-Driven Ferromagnetic Resonance of Individual Nanomagnets, *Phys. Rev. Lett.* **96**, 227601 (2006).
- [108] T. Holstein and H. Primakoff, Field Dependence of the Intrinsic Domain Magnetization of a Ferromagnet, *Phys. Rev.* **58**, 1098 (1940).
- [109] S. Aldana, C. Bruder, and A. Nunnenkamp, Equivalence between an optomechanical system and a Kerr medium, *Phys. Rev. A* **88**, 043826 (2013).